# STUDY OF CHARMED HADRONS LIFETIME WITH 400 GEV PROTONS AT THE CERN-SPS

A THESIS SUBMITTED TO
THE GRADUATE SCHOOL OF NATURAL AND APPLIED SCIENCES
OF
MIDDLE EAST TECHNICAL UNIVERSITY

BY

CANAY ÖZ

IN PARTIAL FULFILLMENT OF THE REQUIREMENTS
FOR
THE DEGREE OF MASTER OF SCIENCE
IN
PHYSICS

SEPTEMBER 2022

Approval of the thesis:

**STUDY OF CHARMED HADRONS LIFETIME WITH 400 GEV PROTONS AT THE CERN-SPS**

submitted by **CANAY ÖZ** in partial fulfillment of the requirements for the degree of **Master of Science in Physics Department, Middle East Technical University** by,

Prof. Dr. Halil Kalıpçılar
Dean, Graduate School of **Natural and Applied Sciences** _____

Prof. Dr. Seçkin Kürkçüoğlu
Head of Department, **Physics** _____

Prof. Dr. Ali Murat Güler
Supervisor, **Physics , METU** _____

**Examining Committee Members:**

Prof. Dr. İsmail Turan
Physics, METU _____

Prof. Dr. Ali Murat Güler
Physics, METU _____

Assist. Prof. Dr. Osamu Sato
Physics, Nagoya University _____

Date:

**I hereby declare that all information in this document has been obtained and presented in accordance with academic rules and ethical conduct. I also declare that, as required by these rules and conduct, I have fully cited and referenced all material and results that are not original to this work.**

Name, Surname: Canay Öz

Signature :

# ABSTRACT

## STUDY OF CHARMED HADRONS LIFETIME WITH 400 GEV PROTONS AT THE CERN-SPS

Öz, Canay
M.S., Department of Physics
Supervisor: Prof. Dr. Ali Murat Güler

September 2022, 54 pages

The Standard Model of particle physics contains three active neutrinos associated to three charged leptons: electron, muon and tau. Electron neutrino and muon neutrino were experimentally observed in 1956 and 1962 respectively but observation of tau neutrino was released at the beginning of 21st century as its observation requires special detection techniques. Only few measurements with limited statistics have been done in order to measure its properties.

The DsTau project at CERN has been proposed to study tau neutrino production aiming precise measurement of tau neutrino production cross section. In addition, the analysis of $2.3 \times 10^8$ proton interactions will yield $10^5$ charmed decay which will allow us to extract many more physical quantities like measurement of charmed hadron lifetime and measurement of interaction lengths of charmed hadrons. In this thesis work, the track reconstruction performance of the DsTau detector has been studied in detail and using a sub-sample of 2018 pilot run, the charmed hadron lifetimes have been obtained with the help of MC simulations. The obtained lifetimes are consistent with PDG values.

Keywords: DsTau experiment, Standard Model, Charmed particles

# ÖZ

## CERN-SPS'DEN GELEN 400 GEV PROTON İLE ÜRETİLEN CHARM KUARK İÇEREN HADRONLARIN ÖMÜRLERİNİN İNCELENMESİ

Öz, Canay
Yüksek Lisans, Fizik Bölümü
Tez Yöneticisi: Prof. Dr. Ali Murat Güler

Eylül 2022 , 54 sayfa

Standart model parçacık fiziği, üç yüklü leptonla ilişkili üç aktif nötrino içerir: elektron, muon ve tau. Elektron nötrino ve muon nötrino, sırasıyla 1956 ve 1962 de deneysel olarak gözlemlendi, ancak tau nötrinosunun gözlemlenmesi, gözlem için özel saptama teknikleri gerektirdiğinden 21. yüzyılın başında gerçekleştirildi. Özelliklerini ölçmek için sınırlı istatistiklere sahip sadece birkaç ölçüm yapılmıştır.

CERN'deki DsTau projesi, tau nötrino üretim kesitinin hassas ölçümünü yapmak amacıyla tau nötrino üretiminin incelenmesi için önerildi. Buna ek olarak, $2.3 \times 10^8$ proton etkileşimlerinin analizi, $10^5$ charm kuark bulunduran hadronların bozunumunu vererek onların ömrünün ölçümü ve etkileşim uzunluklarının ölçümü gibi daha birçok fiziksel niceliği ölçmemize izin verecektir. Bu tez çalışmasında, DsTau dedektörünün iz rekonstrüksiyon performansı detaylı olarak incelenmiş ve 2018 pilot çalışmasının bir bölümü kullanılarak, MC simülasyonları yardımıyla içeriğinde charm kuark bulunduran hadronların ömürleri elde edilmiştir. Elde edilen ömürler PDG değerleri ile uyumludur.

Anahtar Kelimeler: DsTau deneyi, Standart Model, Tılsımlı parçacıklar

To my parents Nesrin and Zeki.

## ACKNOWLEDGMENTS

I gratefully acknowledge TENMAK for supporting our project "Setup and testing of new emulsion-based experiments and physics research beyond the standard model at CERN" (project no: 2022TENMAK(CERN)-A5.H3.F2-1). I would like to thank all members of DsTau collaboration for their suports and sharing their knowledge with me which makes this study possible. I would also like to thank to my dear friends from METU DsTau team; Emin Yüksel, Neşe Ergin and especially Melike Nur Erbek for their kind supports during my study. I would also like to thank all my sincere friends who have been supporting and encouraging me for years including Çiğdem Özcan, Alican Beştemir, Ezgi Beştemir and especially Mert Erözden for his patience in me. Furthermore, I would like to share my special thanks to my brothers Can, Cantürk and Caner, and also my lovely mother and father, Nesrin and Zeki for all their patience and support during my study. Finally yet importantly, I would like to thank Prof. Dr. Ali Murat Güler, who has not only supervised this thesis but also shared his experience, knowledge and wisdom with me.

## TABLE OF CONTENTS

ABSTRACT . . . . . v

ÖZ . . . . . vii

ACKNOWLEDGMENTS . . . . . x

TABLE OF CONTENTS . . . . . xi

LIST OF TABLES . . . . . xiv

LIST OF FIGURES . . . . . xvi

LIST OF ABBREVIATIONS . . . . . xxi

CHAPTERS

1 INTRODUCTION . . . . . 1

2 ELEMENTARY PARTICLES AND CHARMED PARTICLES . . . . . 3

2.1 Elementary particles of Standard Model . . . . . 3

2.1.1 Quarks . . . . . 4

2.1.2 Leptons . . . . . 5

2.1.3 Bosons and fundamental forces . . . . . 6

2.2 Hadrons . . . . . 7

2.2.1 Baryons . . . . . 7

2.2.2 Mesons . . . . . 9

2.3 Charmed particles . . . . . 9

3 DsTau EXPERIMENT . . . . . 13

3.1 Principle of the experiment . . . . . 13

3.2 Detector structure . . . . . 15

3.2.1 Target Mover . . . . . 17

3.2.2 Target Selection . . . . . 17

4 DATA ANALYSIS FOR PILOT RUN AND IMPROVEMENT OF TRACKING . . . . . 19

4.1 Data Analysis for pilot run . . . . . 19

4.1.1 Allignment and Reconstruction . . . . . 20

4.1.2 Tracking . . . . . 22

4.1.3 Vertexing . . . . . 24

4.1.4 Decay Search . . . . . 25

4.2 Improvement of Tracking . . . . . 26

4.2.1 Data samples . . . . . 27

4.2.2 Position and angular resolutions . . . . . 27

4.2.3 $\chi^2$ Results . . . . . 30

5 LIFETIME MEASUREMENT . . . . . 35

5.1 Introduction . . . . . 35

5.2 Data Selection . . . . . 36

5.3 Monte Carlo Simulation . . . . . 39

5.4 Lifetime estimation . . . . . 43

5.5 Results . . . . . 45

6 CONCLUSION . . . . . 51

REFERENCES . . . . . 53

## LIST OF TABLES

TABLES

Table 2.1 Intrinsic quantum numbers of quarks . . . . . 5

Table 2.2 Properties of leptons . . . . . 6

Table 3.1 Momentum efficiency for test beam module and physics run module 17

Table 3.2 Detection efficiency for both 0.5 mm thick Tungsten (W) plates and 1 mm thick Molybdenum (Mo) plates with Monte Carlo data . . . . . 18

Table 4.1 9 Sub volumes according to plate number . . . . . 23

Table 4.2 Processed modules for pilot run of DsTau . . . . . 24

Table 4.3 Number of vertices found and decay search results in tungsten for a sample of data and FLUKA simulation. . . . . 26

Table 4.4 Number of segments and number of tracks in data and MC samples. 27

Table 4.5 Position resolutions for all tracks and for high momentum tracks. . . 29

Table 4.6 Angular resolutions for all tracks and for high momentum tracks. . . 30

Table 4.7 Number of rejected segments and tracks with their percentages with respect to all tracks and segments. . . . . 34

Table 5.1 Selection criteria for double kink $D_s \rightarrow \tau \rightarrow X$ . . . . . 37

Table 5.2 Charm meson distributions of $50 \times 10^6$ double charm events with second charm particle having $c$ quark . . . . . 39

Table 5.3 Charm meson distributions of $50 \times 10^6$ double charm events with second charm particle having $\bar{c}$ anti-quark . . . . . 40

Table 5.4 MC Charm events . . . . . 41

Table 5.5 Selection criteria for pair charm . . . . . 43

Table 5.6 Selection of charmed events for lifetime estimation. . . . . 47

Table 5.7 Distributions of 1-prong charged charm particles selected from generated MC events and lifetime of charged charm particles according to PDG. . . . . 49

## LIST OF FIGURES

FIGURES


Figure 2.1 Structure of matter. . . . . 4

Figure 2.2 The Standard Model of elementary parcticles and their properties. 4

Figure 2.3 Different types of hadrons. . . . . 7

Figure 2.4 Symmetric 20-plet (left) and mixed-symmetric 20-plet (right) for SU(4) baryons. . . . . 8

Figure 2.5 Middle layers of symmetric and mixed-symmetric 20-plets of Fig. 2.4 for baryons containing one charm quark. . . . . 8

Figure 2.6 Meson 16-plet in SU(4). . . . . 9

Figure 2.7 D meson production from p-p collision via gluon fusion. . . . . 10

Figure 2.8 Feynman diagrams of $c$, $\bar{c}$ production from QCD processes. . . . 10

Figure 2.9 Leptonic channel Feynman diagram for $D_s^-$. . . . . 11

Figure 2.10 Semi-leptonic channel Feynman diagram for $D$ meson. . . . . 11

Figure 2.11 Hadronic channel Feynman diagram for $D^0$ meson. . . . . 11

Figure 3.1 $D_s \rightarrow \tau \rightarrow$ X . . . . . 13

Figure 3.2 Kink angle distribution . . . . . 14

Figure 3.3 View of emulsion from different perspectives . . . . . 14

Figure 3.4 Module Structure for test run . . . . . 15

Figure 3.5 Module structure with ECC for test run (top) and with Momentum analyzer for physics run (bottom). . . . . 16

Figure 3.6 Track density comparison with Geant4 simulation of old ECC design and new Momentum analyzer . . . . . 16

Figure 3.7 Photo and schematic of detector structure for test beams and pilot run at CERN SPS H4 beamline . . . . . 17

Figure 3.8 New target mover for the physics run. . . . . 18

Figure 4.1 Number of protons on target vs beam exposure date for each module. . . . . 19

Figure 4.2 Efficiency of finding base-track with respect to the plate number of the track segment. . . . . 21

Figure 4.3 Angular (left) and positional (right) resolutions with respect to track angle. . . . . 22

Figure 4.4 Reconstructed tracks for 2 mm x 2 mm area for 15 plates. . . . . 22

Figure 4.5 Relationship between track density and plate number compared with FLUKA simulation. . . . . 23

Figure 4.6 Distribution of vertices according to Z-direction . . . . . 25

Figure 4.7 Comparison of multiplicty for data and FLUKA simulation . . . 25

Figure 4.8 Double kink example . . . . . 26

Figure 4.9 Calculation of $\Delta X$ and $\Delta Y$ from track fit. . . . . 28

Figure 4.10 Distribution of difference between observed and expected X (Y) positions from track fit in left (right). . . . . 28

Figure 4.11 Distribution of difference between observed and expected X (Y) positions from track fit in left (right) for high momentum tracks. . . . . 28

Figure 4.12 Distribution of difference between observed and expected $\theta_X$ ($\theta_Y$) angles from track fit in left (right) . . . . . 29

Figure 4.13 Distribution of difference between observed and expected $\theta_X$ ($\theta_Y$) angles from track fit in left (right) for high momentum tracks . . . 30

Figure 4.14 $\Delta X^2/{\sigma_X}^2$ (left) and $\Delta Y^2/{\sigma_Y}^2$ (right) distributions with position resolutions from Table 4.5. . . . . 31

Figure 4.15 $\Delta {\theta_X}^2/{\sigma_{\theta_X}}^2$ (left) and $\Delta {\theta_Y}^2/{\sigma_{\theta_Y}}^2$ (right) distributions with angular resolutions from Table 4.6. . . . . 31

Figure 4.16 $\Delta X^2/{\sigma_X}^2$ (left) and $\Delta Y^2/{\sigma_Y}^2$ (right) distributions with position resolutions from Table 4.5 for high momentum tracks. . . . . 31

Figure 4.17 $\Delta {\theta_X}^2/{\sigma_{\theta_X}}^2$ (left) and $\Delta {\theta_Y}^2/{\sigma_{\theta_Y}}^2$ (right) distributions with angular resolutions from Table 4.6 for high momentum tracks. . . . . 32

Figure 4.18 $\chi^2$ distribution from resolutions obtained by all tracks between 0-10 (left) and 0-20 (right). . . . . 32

Figure 4.19 $\chi^2$ distribution from resolutions obtained by high momentum tracks. . . . . 33

Figure 4.20 $\chi^2$ distribution of segments that has larger $\chi^2$ than acceptance threshold. . . . . 33

Figure 5.1 Decay topology of $D_s$. . . . . 35

Figure 5.2 Event display of a charmed decay candidate. . . . . 37

Figure 5.3 Slope distributions in X-direction (left) and in Y-direction (right) for 1-prong events. . . . . 38

Figure 5.4 Slope distributions in X-direction (left) and in Y-direction (right) for 2-prong events. . . . . 38

Figure 5.5 Flight length distributions for 1-prong (left) and 2-prong (right) events. . . . . 38

Figure 5.6 Kink angle distribution for 1-prong events (left) and opening angle distribution for 2-prong events (right). . . . . 39

Figure 5.7 PDG code of charm particles for 1-prong (left) and 2-prong (right) events. . . . . 40

Figure 5.8 Flight length distributions for 1-prong (left) and 2-prong (right) MC events. . . . . 41

Figure 5.9 Kink angle distribution for 1-prong (left) and opening angle distribution for 2-prong (right) for Monte Carlo events. . . . . 42

Figure 5.10 Calculated Lifetime distributions for 1-prong (left) and 2-prong (right) for MC events. . . . . 42

Figure 5.11 Estimation for sample 1-prong charm particle which has 3.634 mm of flight length and 0.08434 rad kink angle. . . . . 44

Figure 5.12 Estimation of lifetime for sample 1-prong charm particle which has 3.634 mm of flight length and 0.08434 rad kink angle. . . . . 44

Figure 5.13 Estimation for sample 2-prong neutral charm particle which has 2.334 mm of flight length and 0.03895 rad opening angle. . . . . 45

Figure 5.14 Estimation of Life Time for sample 2-prong neutral charm particle which has 2.334 mm of flight length and 0.03895 rad opening angle. 45

Figure 5.15 Flight length distributions with selection criteria (Table 5.5) for 1-prong . . . . . 46

Figure 5.16 Kink angle distributions with selection criteria (Table 5.5) for 1-prong. . . . . 46

Figure 5.17 Flight length distributions with selection criteria (Table 5.5) for 2-prong . . . . . 47

Figure 5.18 Opening angle distributions with selection criteria (Table 5.5) for 2-prong . . . . . 47

Figure 5.19 Lifetime distribution without selection criteria for 1-prong (left) and for 2-prong (right). . . . . 48

Figure 5.20 Lifetime distribution with selection criteria applied for 1-prong (left) and for 2-prong (right). . . . . 48

## LIST OF ABBREVIATIONS

| | |
|---|---|
| DONuT | Direct Observation of Nu-Tau |
| SM | Standard Model |
| CC | Charged Current |
| NC | Neutral Current |
| DsTau | The DsTau (NA65) Collaboration |
| METU | Middle East Technical University |
| CERN | the European Organization for Nuclear Research |
| CKM | Cabibbo-Kobayashi-Maskawa |
| TRUBA | Turkish Science e-Infrastructure |
| OPERA | The Oscillation Project with Emulsion-tRacking Apparatus |
| MC | Monte Carlo |
| HTS | Hyper Track Selector |
| ECC | Emulsion Cloud Chamber |
| PDG | Particle Data Group |

# CHAPTER 1

# INTRODUCTION

Fundamental particles and their interactions are explained well with the Standard Model (SM) of the particle physics. Although SM has been developed in early 1970s, it has been tested by many experiments and its predictions are well consistent with the experimental measurements until today [1]. As the experimental techniques and data statistics are improved in time more precise measurements will be performed to search for physics beyond SM. In particular, many theories suggest violation of lepton universality which is a basic assumption of SM. Lepton universality suggests flavour independence for all three lepton flavor [2]. Even though there are many energy frontier experiments which are focusing on particles with high masses, to test lepton universality of small mass particles like neutrinos, intensity frontier experiments are needed to accumulate more data to search for such processes.

The DsTau (NA65) collaboration at CERN is established to study tau neutrino production via $D_s$ decays. Having known the tau neutrino production cross-section accurately will reduce uncertainty in tau-neutrino cross-section measurements. In addition, precise measurement of the tau neutrino flux in accelerator experiments will allow to study physics beyond SM such as testing lepton universality. The precise knowledge of tau neutrino production cross-section has significant impact on the future neutrino experiments like the SHiP project at CERN [3].

The METU DsTau team is a part of the DsTau collaboration since the beginning and contributes in many different aspects of the experiment. The DsTau experiment uses 400 GeV proton beam from CERN Super Proton Synchrotron (SPS) accelarator to observe $D_s$ to $\tau$ decays. The topology of $D_s$ to $\tau$ to X decay, has a unique signature as charm quarks generated in pairs and both $D_s$ and $\tau$ decays with short flight

lengths in order of millimetres. Both short flight lengths and very small kink angle of $D_s$ to $\tau$ decay bring technical difficulties for the detection. To detect this decay topology DsTau use an emulsion particle detector which provides sub-micron spatial resolution.

The analysis of 2.3 $\times$ $10^8$ proton interactions in the DsTau experiment will result in $10^5$ charm decays which offer very rich physics. In the DsTau experiment pilot run was performed in 2018. Emulsion films of pilot runs were scanned and event reconstruction and analysis are on-going. A sub-sample of the pilot run data was analysed to estimate lifetime of the charmed mesons. The structure of this thesis can be summarized as;

- In Chapter 2, an introduction to fundamental particles and Standard model will be given.
- A detailed detector structure of the DsTau experiment and principles of the experiment will be described in Chapter 3.
- Data analysis for pilot run and improvement of tracking will be explained in Chapter 4.
- In Chapter 5, the lifetime measurement of charmed particles by using test beam data and MC simulations will be explained in detail.
- Summary of the measurement and conclusions of this analysis will be given in Chapter 6.

# CHAPTER 2

# ELEMENTARY PARTICLES AND CHARMED PARTICLES

## 2.1 Elementary particles of Standard Model

A matter encountered in our daily life can be explained by molecules and atoms but to be able to understand the matter in the universe particles need further investigation. Atoms are made of nuclei and electrons and inside the nuclei there are protons and neutrons (Figure 2.1). Neither protons and neutrons nor electrons are alone in their categories. Instead protons and neutrons are not elementary particles any more because of their quark structure. Each proton and neutron are consist of three quarks. To be able to understand how universe works, it is not only enough to investigate particles but it is also needed to understand how they interact with each other. SM of the particle physics, not only describes particles and their structure but also describes their interactions via three fundamental forces namely electromagnetic, weak and strong forces [4].

In SM, particles are classified as fermions and bosons (Figure 2.2).While fermions are spin half particles, bosons have integer spin. Fermions include quarks and leptons, which are associated with matter while Bosons are called force carries in SM. Also fermions can be divided into two categories as quarks and leptons [5]. There are also antiparticles, which have the same mass as normal particles but have opposite quantum numbers, associated for each of leptons and quarks. There are three generations for each category, first generation of quarks are up ($u$) and down ($d$) quarks and their anti particles which are also building blocks of protons ($p$) and neutrons ($n$). Protons ($uud$) are made up of 2 up quarks and 1 down quarks while neutrons ($udd$) are made up from 2 down quarks and 1 up quark. The first generation of leptons, consists of

electron ($e^-$) and electron neutrino ($\nu_e$) and their anti-particles.

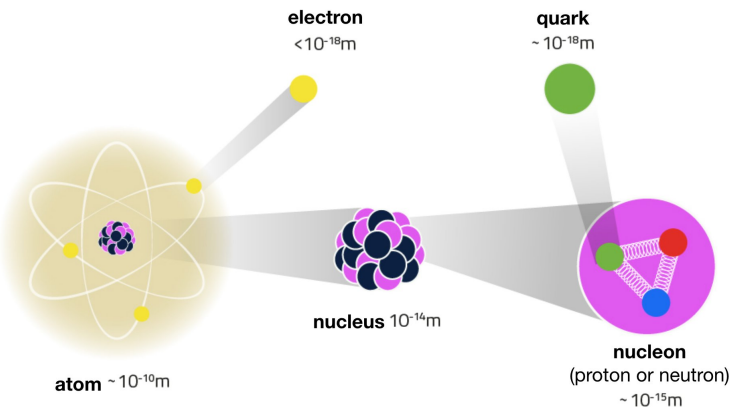


Figure 2.1: Structure of matter.

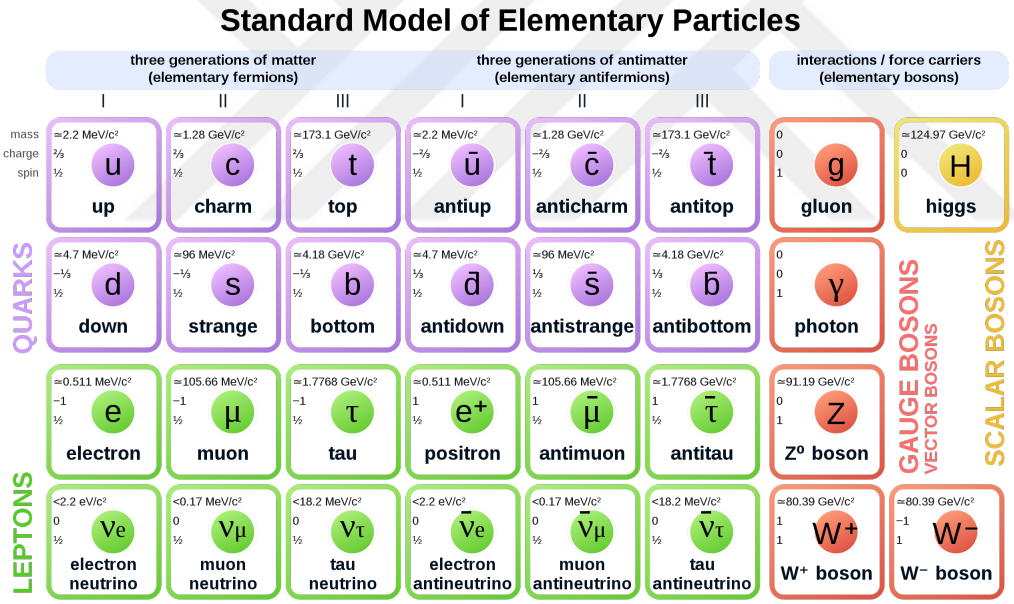


Figure 2.2: The Standard Model of elementary parcticles and their properties.

### 2.1.1 Quarks

There are three generations of quarks where the first generation is made up from up and down quarks while the second generation consists of charm ($c$) and strange ($s$)

quarks and their anti-particles. With increasing number of generations the masses of the quarks are getting heavier and the third generation quarks top ($t$) and bottom ($b$) are the heaviest quarks. Quarks can interact with all four fundamental forces and have intrinsic quantum numbers as electric charge, color charge, spin, mass, charm, strangeness, topness, bottomness described by Table (2.1). Quarks can have electric charge of $-1/3$ and $2/3$ and opposite of these electric charges for their anti-particles.

Table 2.1: Intrinsic quantum numbers of quarks

| Property - Quark | $d$ | $u$ | $s$ | $c$ | $b$ | $t$ |
|---|---|---|---|---|---|---|
| $Q$ - electric charge | $-1/3$ | $2/3$ | $-1/3$ | $2/3$ | $-1/3$ | $2/3$ |
| $I$ - isospin | $1/2$ | $1/2$ | $0$ | $0$ | $0$ | $0$ |
| $S$ - strangeness | $0$ | $0$ | $-1$ | $0$ | $0$ | $0$ |
| $C$ - charm | $0$ | $0$ | $0$ | $+1$ | $0$ | $0$ |
| $B$ - bottomness | $0$ | $0$ | $0$ | $0$ | $-1$ | $0$ |
| $T$ - topness | $0$ | $0$ | $0$ | $0$ | $0$ | $+1$ |

Charm number which should be conserved in strong interactions has an importance for this study. This is the reason behind the search for charmed particles in pair from the proton-matter interactions of the DsTau experiment where one of the charmed particles must contain anti-charm quark while the other one contains charm quark.

### 2.1.2 Leptons

Leptons are also divided into three generations like quarks. While first generation consists of electron and electron neutrino. For second and third generations there are muon ($\mu^-$), muon neutrino ($\nu_\mu$), tau ($\tau$) and tau neutrino ($\nu_\tau$). While all electron, muon and tau have electric charge $-1$, neutrinos does not carry electric charge. Also one important difference between quarks and leptons are that leptons do not interact with strong force thus they do not have color charges. But similar to quarks lepton number must be conserved in all interactions. Properties of leptons are summarized in Table(2.2) [6].

Table 2.2: Properties of leptons

| Lepton - Property | Mass $[MeV/c^2]$ | Electric Charge $(e)$ | Spin $(S)$ | Lepton number $(L)$ | Electron lepton number $(L_e)$ | Muon lepton number $(L_\mu)$ | Tau lepton number $(L_\tau)$ |
|---|---|---|---|---|---|---|---|
| Electron - $e^-$ | 0.511 | $-1$ | $1/2$ | $+1$ | $+1$ | 0 | 0 |
| Electron Neutrino - $\nu_e$ | $< 210^{-6}$ | 0 | $1/2$ | $+1$ | $+1$ | 0 | 0 |
| Muon - $\mu$ | 105.66 | $-1$ | $1/2$ | $+1$ | 0 | $+1$ | 0 |
| Muon Neutrino - $\nu_\mu$ | $< 210^{-6}$ | 0 | $1/2$ | $+1$ | 0 | $+1$ | 0 |
| Tau - $\tau$ | 1776.86 | $-1$ | $1/2$ | $+1$ | 0 | 0 | $+1$ |
| Tau Neutrino - $\nu_\tau$ | $< 210^{-6}$ | 0 | $1/2$ | $+1$ | 0 | 0 | $+1$ |

### 2.1.3 Bosons and fundamental forces

Bosons are spin integer particles that mediate fundamental forces in SM. While gluon $(g)$ and photon $(\gamma)$ which are carriers of Strong and Electromagnetic forces are massless other bosons have mass.

Gluons are the force carriers of Strong force and they can interact with each other with their color charges. As leptons do not carry color charge they can not interact with strong force. At very small distances like in the nuclei or inside a proton strong force is the dominant force and it is effective force for quark confinement. Quark confinement is the reason why there is no way to observe free quarks and it is described by Quantum Chromodynamics (QCD) in SM.

Unlike gluon, $W^\pm$ and $Z^0$ have mass and they are carriers of Weak force. Both quarks and leptons can interact with Weak force. There are two types of Weak interactions that can undergo by two different bosons $W^\pm$ and $Z^0$ which are charged-current interaction and neutral-current interaction. As $W^\pm$ has electric charge it is the only boson that can change the electric charge of a lepton or a quark. In charged-current interaction an electron, muon or tau will absorb a $W^+$ and will be converted to neu-

trino. To conserve electron lepton number, muon lepton number or tau lepton number outgoing neutrino must be in the same generation. Unlike lepton when a quark undergo charged-current interaction, it can change the generation for example when a $u$ quark absorbs $W^-$ it can be converted to $d$, $s$ or $b$ quarks and the probability of this conversion can be explained by Cabibbo-Kobayashi-Maskawa (CKM) matrix [7].

Photon ($\gamma$) is the force carrier of Electromagnetic force and this interaction is formulated as Quantum Electro Dynamics (QED) in SM. Together with Weak force these two forces can be unified and understood as a single interaction after the Glashow-Weinberg-Salam theory [8].

## 2.2 Hadrons

Hadrons are particles consists of quarks and anti-quarks and they can be divided into three categories which are Baryons and Mesons and Exotic hadrons (Figure2.3). Baryons consist of three quarks or three antiquarks and mesons are bound state of a quark and an anti-quark. Exotic hadrons are the bound states of four or more quarks and can be named as Tetra-quark and Penta-quark structures.

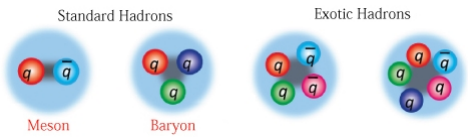


Figure 2.3: Different types of hadrons.

### 2.2.1 Baryons

Baryons made up from 3 quarks ($qqq$ or $\bar{q}\bar{q}\bar{q}$). Each quark adds $1/3$ to Baryon number and each anti-quark adds $-1/3$ to Baryon number. Thus baryons have Baryon number of $+1$ or $-1$. The structure of Baryons can be explained through color charges which are "red", "blue" and "green". All strongly interacting particles are color-singlet. Baryon properties are described via SU(3) flavor group, which belongs to the multiplets shown by right of Eq(2.1) [9]. Here S is symmetric, M is mixed-symmetry

and A is antisymmetric. Similarly if charm quark ($c$) is added, it can be explained by SU(4) multiplets and these multiplets can be explained by Eq(2.2), and shown more detailed in Figure(2.4). Middle layers of both 20-plet shows the baryons that contain one charm quark. Due to their importance for this thesis, charmed baryons are shown more detailed in Figure(2.5).

$$\mathbf{3} \otimes \mathbf{3} \otimes \mathbf{3} = \mathbf{10}_S \oplus \mathbf{8}_M \oplus \mathbf{8}_M \oplus \mathbf{1}_A \tag{2.1}$$

$$\mathbf{4} \otimes \mathbf{4} \otimes \mathbf{4} = \mathbf{20}_S \oplus \mathbf{20}_M \oplus \mathbf{20}_M \oplus \mathbf{4}_A \tag{2.2}$$

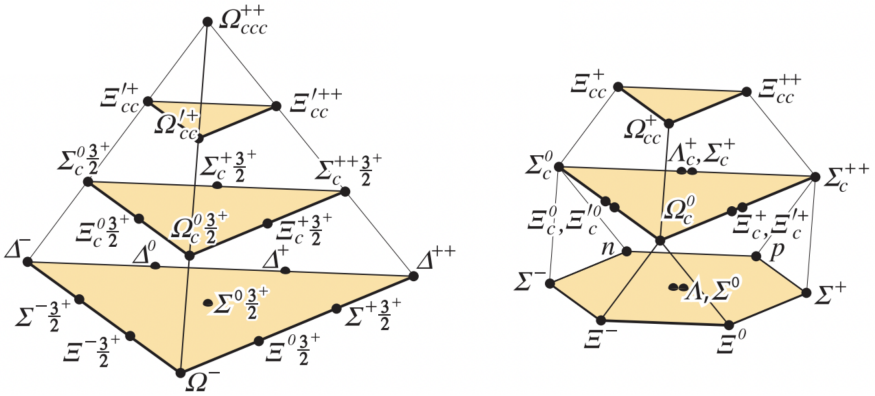


Figure 2.4: Symmetric 20-plet (left) and mixed-symmetric 20-plet (right) for SU(4) baryons.

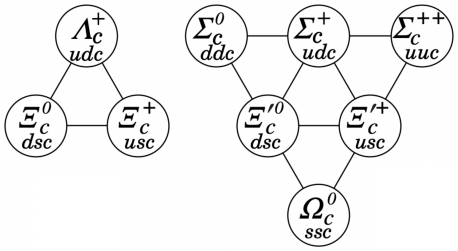


Figure 2.5: Middle layers of symmetric and mixed-symmetric 20-plets of Fig. 2.4 for baryons containing one charm quark.

### 2.2.2 Mesons

A meson consists of one quark and one anti-quark. Thus their baryon number are zero. If a meson can consist of four flavours; $u$, $d$, $s$ and $c$ quark, it can be explained by SU(4) with multiplets by Eq(2.3) and can be shown more detailed in Fig(2.6). Multiplets drawn according to the Isospin ($I$), Charm ($C$) and Hypercharge ($Y$) of the meson (Eq(2.4)) where $B$ is the baryon number, $S$ is the strangeness and $C$ is the charm.

$$\mathbf{4} \otimes \bar{\mathbf{4}} = \mathbf{15} \oplus \mathbf{1} \tag{2.3}$$

$$Y = S + B - \frac{C}{3} \tag{2.4}$$

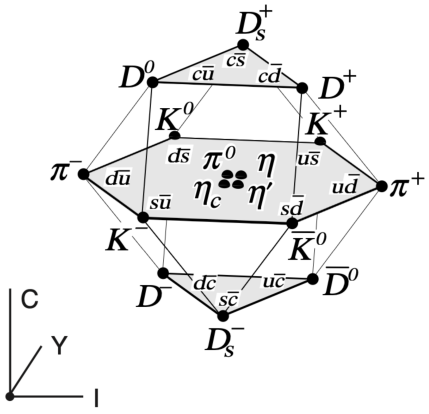


Figure 2.6: Meson 16-plet in SU(4).

## 2.3 Charmed particles

Charmed mesons in top and bottom layers of meson 16-plet (Figure 2.6) are formed through hadronization process in which quarks and gluons combine to form hadrons [10]. An example for this process can be found in Figure (2.7).

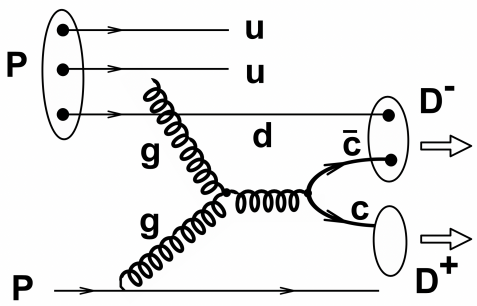


Figure 2.7: D meson production from p-p collision via gluon fusion.

Charm hadronization can be summarized in 3 steps. In first step two protons collide with high energy [11]. After the collision there will be many free partons in the environment which will then interact via strong force in the second step. QCD effects the process of charm quark pair production (Feynman diagrams for possible processes show in Figure 2.8). In third step, charm quarks interact with strong force with other free partons to form bound states which are charmed mesons and baryons like $D^+$, $D^-$, $D^0$, $D_s^-$, $D_s^+$, $\Lambda_c^+$ and $\Xi_c^+$.

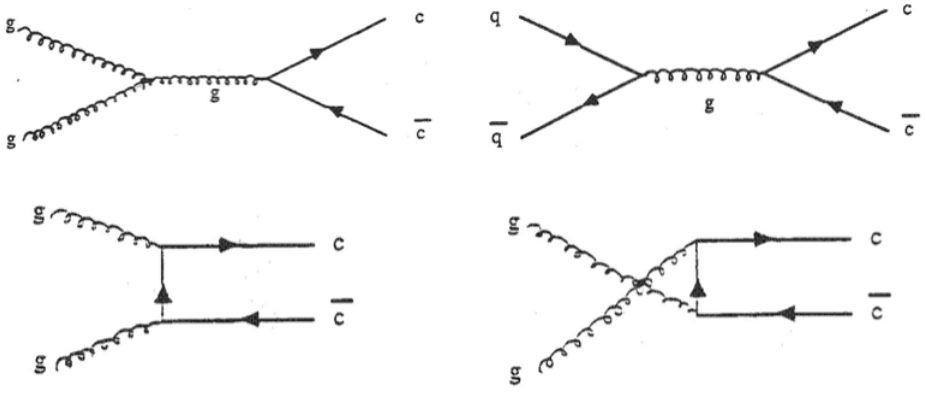


Figure 2.8: Feynman diagrams of $c$, $\bar{c}$ production from QCD processes.

Charmed mesons can decay with purely leptonic channel, hadronic channel or semi-leptonic channels [12]. In leptonic channel D meson will emit a W boson to decay into a lepton and neutrino which is described by an example in Figure (2.9) [13].

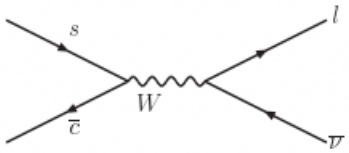


Figure 2.9: Leptonic channel Feynman diagram for $D_s^-$.

In semi-leptonic channel charmed meson will decay into another meson, a lepton and neutrino while in hadronic channel decay products will be only hadrons.

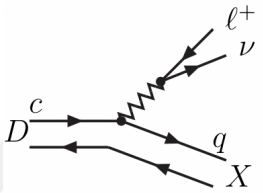


Figure 2.10: Semi-leptonic channel Feynman diagram for $D$ meson.

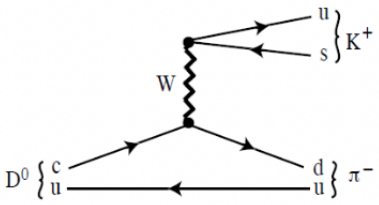


Figure 2.11: Hadronic channel Feynman diagram for $D^0$ meson.

In the DsTau experiment, the nuclear emulsion techniques allow us to study production and decay of the charmed particles with a high precision. For example, $D_s$ differential production cross section and $D_s$ decay branching can be measured at the same time. The neutral and charged charmed hadrons and their decay topologies can be studied in detail.

# CHAPTER 3

# DsTau EXPERIMENT

## 3.1 Principle of the experiment

The main aim of the DsTau experiment is to measure the differential cross-section of $D_s$ with a consecutive decay to tau lepton in p-A interactions at the CERN-SPS. For that purpose, DsTau will collect $2.3 \times 10^8$ p-A interactions to detect about $10^3$ $D_s \rightarrow \tau$ decays. The measurement of DsTau will reduce the systematic error in tau neutrino charged-current cross-section to few % level. Tau neutrinos are produced in Ds and tau decays as shown in Equations (3.1) and (3.2).

$$D_s^+ \rightarrow \tau^+ \nu_\tau \rightarrow X \nu_\tau \bar{\nu_\tau} \tag{3.1}$$

$$D_s^- \rightarrow \tau^- \bar{\nu_\tau} \rightarrow X \bar{\nu_\tau} \nu_\tau \tag{3.2}$$

The DsTau experiment will detect $D_s$ decay from its unique decay topology. This double kink topology is demonstrated more detailed in Figure 3.1 . $D_s$ and $\tau$ decay with a mean flight length of 3.3 mm and 2.0 mm respectively [3]. As charm quarks produced in pairs, another charmed particle will decay with a few mm of flight length.

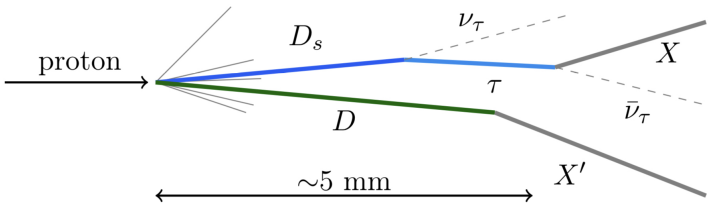


Figure 3.1: $D_s \rightarrow \tau \rightarrow$ X

One technical challenge for this measurement is the very small kink angle of $D_s$ decay. Other one is small decay flight lengths of $D_s$ and $\tau$. The mean of the kink angle of $D_s$ decay is about few mrad (Figure 3.2). Detecting this signal in small volume will require very high precission tracking detector. The emulsion based detector can provide the required resolution for the detection of this unique decay topology [14].

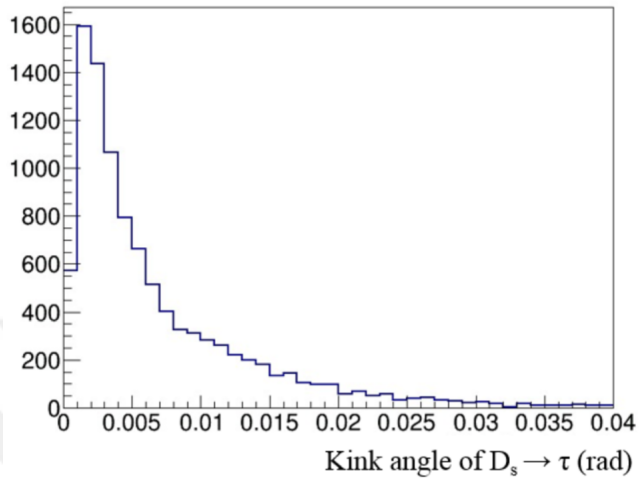


Figure 3.2: Kink angle distribution

Emulsion films (Figure 3.3) are composed from two layers of 44 $\mu$m thick emulsion layers in between a 200 $\mu$m thick plastic layer. The sensitized silver bromide crystals dispersed in gelatin have 2.5 eV band gap and their diameter is 0.2 $\mu$m. Once a charged particle passes through, the ionization is recorded quasi-permanently, and then amplified and fixed by the chemical process. An emulsion detector with 0.2 $\mu$m crystals has a position resolution of 50 nm. An emulsion film structure like ours have an intrinsic angular resolution of 0.35 mrad. This allow us to set a kink detection threshold of 2 mrad at the 4 $\sigma$ confidence level.

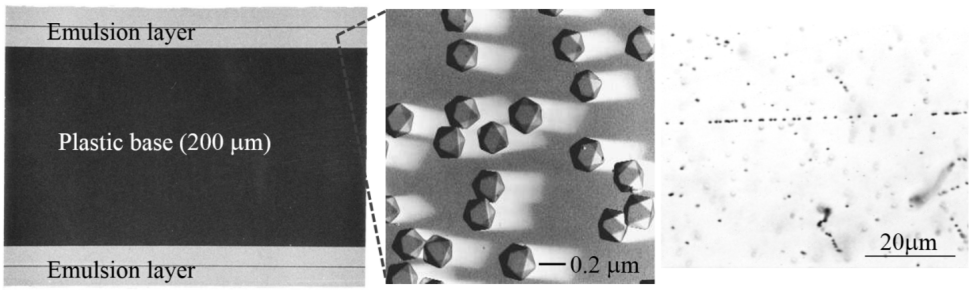


Figure 3.3: View of emulsion from different perspectives

### 3.2 Detector structure

The structure of the DsTau detector for test run (2018) consists of two parts (Figure 3.4). First part has 10 units of 0.5 mm tungsten target followed by 10 emulsion films and 9 plastic layers of 0.2 mm. The second part named as Emulsion Cloud Chamber (ECC), which consists of 26 plates of 1 mm lead and 26 emulsion films between them. The momentum of charged particle is measured by Multiple Coulomb Scattering (MCS) in ECC. Three more emulsion films will be placed in front of the module as a veto plane to tag proton beam. To sum up a module consists of 10 0.5 tungsten layers, 129 emulsion layers, 90 plastic layers and 26 lead plates. The size of the module is 12.5 cm $\times$ 10 cm $\times$ 8.6 cm.

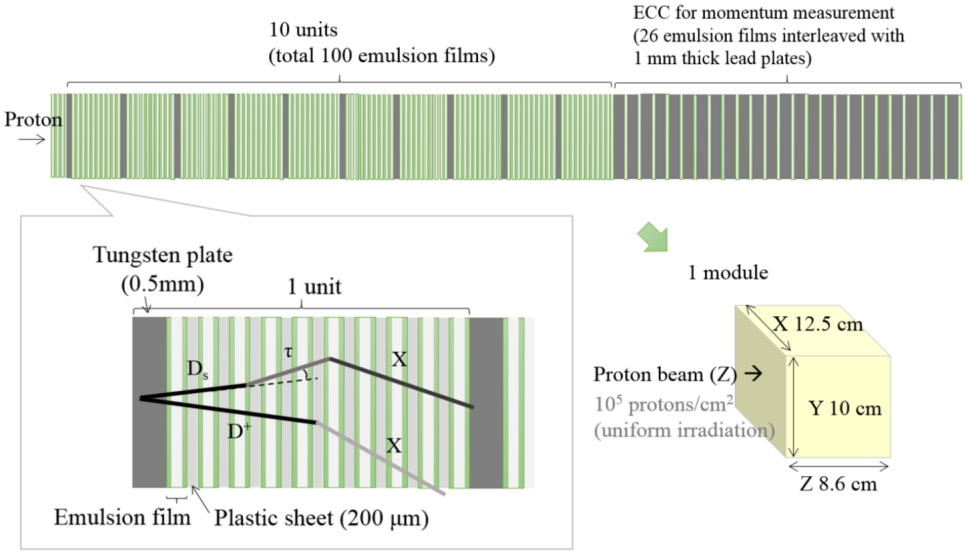


Figure 3.4: Module Structure for test run

After the test run, the size of the emulsion film was changed from 12.5 cm x 10 cm to 25 cm x 20 cm in order to have efficient emulsion scanning and vertex reconstruction. In addition the momentum analyzer part was also upgraded; instead of lead plates, 3 tungsten plates and 25 emulsion plates are used for the momentum measurement (Figure 3.5).

This change in momentum analyzer stucture necessary due to the high track density in the ECC. As electromagnetic shower develops in the dense ECC. So, 26 lead plates

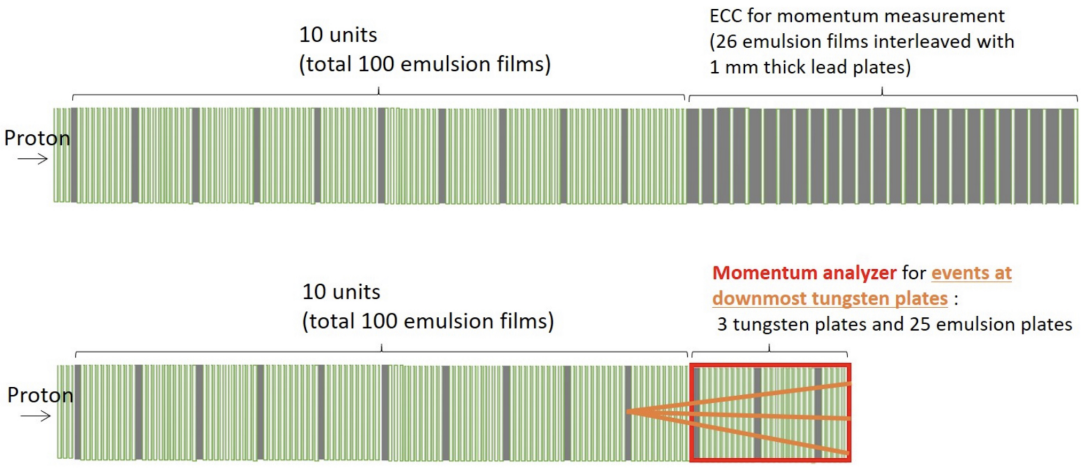


Figure 3.5: Module structure with ECC for test run (top) and with Momentum analyzer for physics run (bottom).

are replaced by 3 plates of 0.5 mm tungsten plates and 25 emulsion plates. By reducing the material density will apparently decrease the track density and will speed up emulsion scanning and analysis (Figure 3.6). Momentum measurement resolution is compared for both designs in Table 3.1.

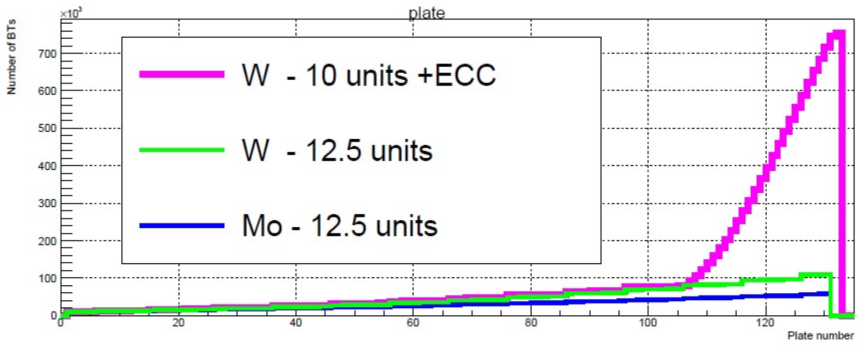


Figure 3.6: Track density comparison with Geant4 simulation of old ECC design and new Momentum analyzer

The emulsion detector and its readout system can operate at a track density up to about $10^6$ particles/cm$^2$, which limits the proton density at the upstream surface of the module to less than $10^5$/cm$^2$. Therefore, 368 modules are needed to collect enough number of proton interactions.

Table 3.1: Momentum efficiency for test beam module and physics run module

| | Original: lead emulsion ECC | New: additional tungsten units |
|---|---|---|
| Structure | 25 1mm lead, 26 emulsion plates | 3 0.5mm tungsten, 25 emulsion plates |
| Momentum resolution | 20 - 40% (upstream ev.)<br>20 - 40% (downstream ev.) | 15 - 40% (upstream ev.)<br>35 - 45% (downstream ev.) |
| Weight | 15.0 kg | 2.4 kg |

### 3.2.1 Target Mover

In order to have a uniform proton radiation, modules are placed to a target mover. The target mover has two step motors to change the position of module with respect to beam. For this purpose it is controlled by a Raspberry PI which changes the position of the module when it receives the SPS timing signal. For the test beam campaigns held in 2016 and 2017 and the pilot run held in 2018, target mover in the Figure (3.7) is used. For physics run size of the emulsion films are increased to 25 cm × 20 cm from 12.5 cm × 10 cm. Thus a larger target mover is needed. For this purpose a target mover used in the J-PARC E07 experiment was provided and modified as shown in Figure (3.8).

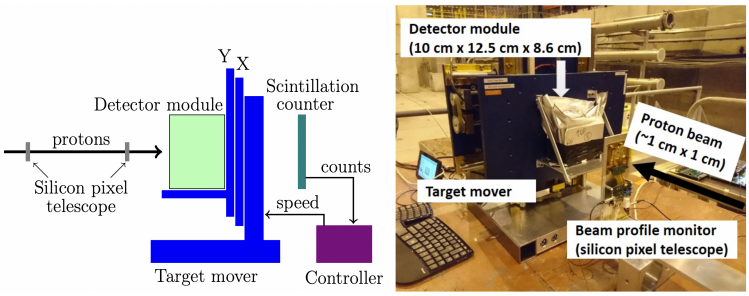


Figure 3.7: Photo and schematic of detector structure for test beams and pilot run at CERN SPS H4 beamline

### 3.2.2 Target Selection

For test runs in 2016 and 2017 and for the pilot run in 2018, 0.5 mm thick tungsten plates are used as a target. Tungsten was also used in DONuT experiment [15] and it

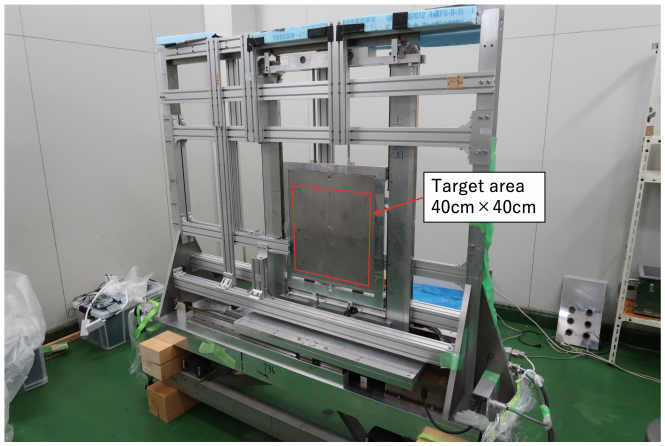


Figure 3.8: New target mover for the physics run.

will also used in the SHiP project. In addition to Tungsten, Molybdenum target will also be used in DsTau physics runs.

Table 3.2: Detection efficiency for both 0.5 mm thick Tungsten (W) plates and 1 mm thick Molybdenum (Mo) plates with Monte Carlo data

| Target | # of proton on target | # of proton interactions | charm pair production | $D_s \to \tau \to$ X |
|---|---|---|---|---|
| 0.5 mm Tungsten plate | $2.15 \times 10^9$ | $1.08 \times 10^8$ | $1.95 \times 10^5$ | 528 |
| 1 mm Molybdenum plate | $2.15 \times 10^9$ | $1.41 \times 10^8$ | $2.10 \times 10^5$ | 498 |

Molybdenum has nearly half of weight density of Tungsten. This difference in density results in using 1 mm thick Molybdenum which is 2 times thick of Tungsten target. But this change in thickness of target can decrease detection efficiency. A test for comparison of detection efficiency is done with a MC simulation for both targets. For both cases $2.15 \times 10^9$ protons are sent to targets and it is assumed for both cases to have same number of plates and emulsion films. The detection efficiency of $D_s \to \tau$ with 0.5 mm thick Tungsten plate is measured as 21.1% while similarly detection efficiency with 1 mm thick Molybdenum plate is measured as 18.4%. This shows that there is no significant differences in using Tungsten or Molybdenum target. The results of MC simulation are summarized in Table 3.2.

# CHAPTER 4

# DATA ANALYSIS FOR PILOT RUN AND IMPROVEMENT OF TRACKING

## 4.1 Data Analysis for pilot run

In 2018, a pilot run was carried out to test each step of the experiment from emulsion production to data analysis. The collected data corresponds to 10% data of the physics run. In this run, about 4000 emulsion film were used to construct 30 emulsion modules (Figure 4.1). The set up was located at the H4 beamline at CERN.

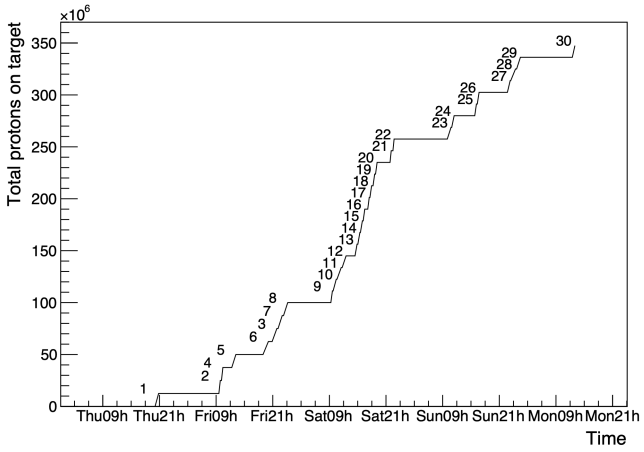


Figure 4.1: Number of protons on target vs beam exposure date for each module.

After the exposure, modules are disassembled at CERN and emulsion films are developed through a chain of chemical processes. After removing silver grains on the surface, the films are ready for scanning which are performed by Hyper Track Selector (HTS) at Nagoya University in Japan.

The data analysis in DsTau consists of four main steps;

- Allignment and Reconstruction
- Tracking
- Vertexing
- Decay Search

In order to detect a few mrad kink angle of $D_s$ to $\tau$ decays, all these steps must applied carefully. In the following these steps will described in detail.

### 4.1.1 Allignment and Reconstruction

As a pilot detector, 30 modules were assembled and exposed to the proton beam. After developing phase, emulsion films were sent to Nagoya for scanning. The scanning of emulsion films were completed in Nagoya and the data processing are going smoothly. For data processing computing centers within the collaboration and CERN are used. Each base track has position information for 3 directions x, y and z and also have slopes regarding to z direction for x, y and z directions (Eq.4.1). Slopes can be defined as a 3D vector $\vec{V}$ as in equation (4.2).

$$\vec{X} = (x, y, z) \tag{4.1}$$

$$\vec{V} = (tan\theta_X, tan\theta_X, 1) \tag{4.2}$$

Due to high track density in DsTau experiment reconstruction of base-tracks can not be done by previous reconstruction tools by older experiments like OPERA. Previous experimental algorithms have difficulty resolving tracks with similar angles within few mrad and with near positions around few micrometers. Due to high track density, misalignment tolerances are decreased, for positional tolerance from 5 $\mu$m to 2.25 $\mu$m and for angular tolerance to lower than 50 mrad. Also angular tolerance is increased

as a function of angle. Moreover a new program is developed to check positional alignment using beam trajectories for high track densities like DsTau experiment.

Due to high track density in down stream plates, base-track detection efficiency decreases by the plate number for each module and this efficiency for each module shown in Figure (4.2). Finding base-track efficiency is higher than 95 % which confirms high efficiency in track detection [16].

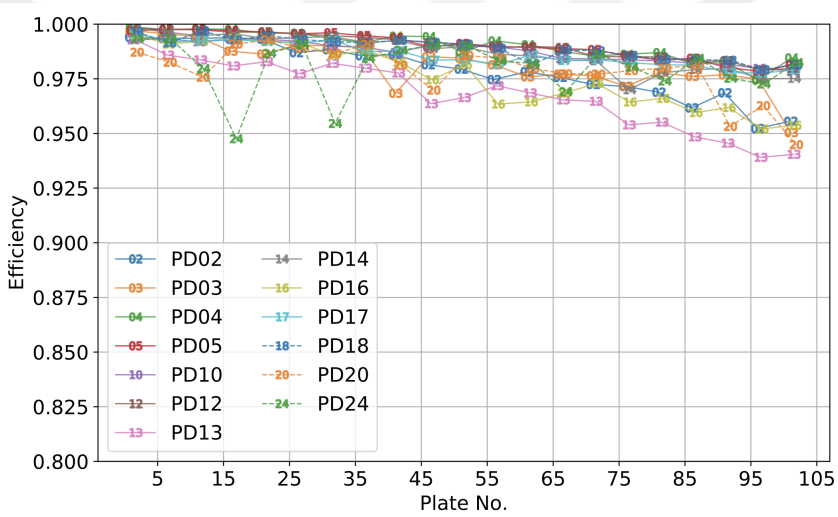


Figure 4.2: Efficiency of finding base-track with respect to the plate number of the track segment.

From tracks that penetrates at least four films, resolutions for angle and position are calculated. Both positional and angular resolutions increase by track angle. For tracks with slope $\leq 0.1$ rad, angular resolution is 2 mrad while positional resolution is 0.56 $\mu$m. Connection between resolutions and track angle is shown in Figure (4.3).

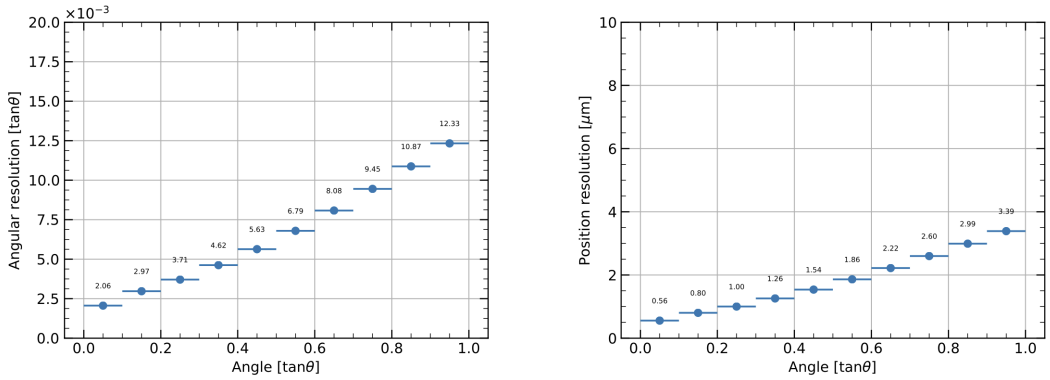


Figure 4.3: Angular (left) and positional (right) resolutions with respect to track angle.

### 4.1.2 Tracking

Tracking is done by linking micro-tracks from different plates together using their position and angular parameters. Figure(4.4) show an example of reconstructed tracks in 2 x 2 $mm^2$ area and it consists about 20 thousand tracks. The track density increases with respect to plate number due to the secondary interactions and electromagnetic shower development (Figure4.5).

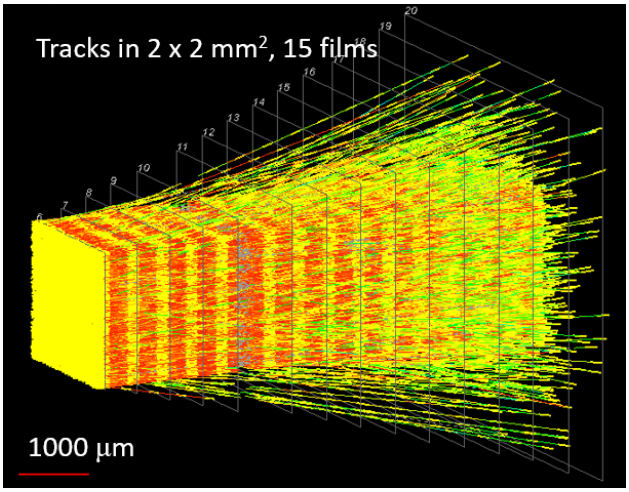


Figure 4.4: Reconstructed tracks for 2 mm x 2 mm area for 15 plates.

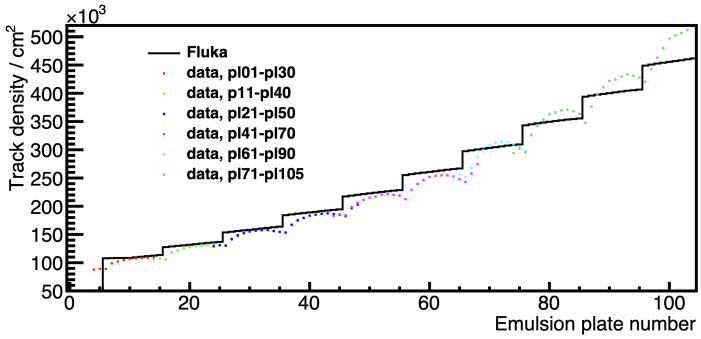


Figure 4.5: Relationship between track density and plate number compared with FLUKA simulation.

Tracking is done by sub-volumes due to high requirement of computational power. Sub-volumes divide scanned area by 1.7 x 1.7 $cm^2$ in X and Y directions with 0.1 cm overlapping sections in both sides. For test run, emulsions with 12.5 cm x 10 cm are used which corresponds to 63 sub-volumes (9 x 7 sub-volumes). In addition to division in sub-volumes, it is only possible to reconstruct 30 to 35 plates at a time again because of computational requirements. For this purpose modules are divided into 8-9 volumes with overlapping 20 plates. This is done by Table (4.1).

Table 4.1: 9 Sub volumes according to plate number

| # of volume | 1 | 2 | 3 | 4 | 5 | 6 | 7 | 8 | 9 |
|---|---|---|---|---|---|---|---|---|---|
| Plate number | 1-30 | 11-40 | 21-50 | 31-60 | 41-70 | 51-80 | 61-90 | 71-100 | 81-105 |

Tracking is done for 16 of 30 modules from 2018 test run. Even though each module is divided into 500-600 sub-volumes, tracking still needs a computing server with at least 128 GB of ram dedicated due to high track density. In addition to Nagoya/Kyushu, ISS and JINR computing servers, computing servers and storage space are allocated from Turkish Science e-Infrastructure (TRUBA) for contributions of Middle East Technical University (METU). Sizes of processed modules, their place of process and efficiencies are given in Table(4.2)

Table 4.2: Processed modules for pilot run of DsTau

| Module Number | Processed place | Size in TB | $\frac{\#Badreconstruction}{\#All}$ sub-volumes ratio |
|---|---|---|---|
| PD02 | Nagoya/Kyushu | 6.0 | 7.9 % |
| PD03 | Nagoya/Kyushu, ISS | 6.6 | 8.3 % |
| PD04 | Nagoya/Kyushu | 8.3 | 20.6 % |
| PD05 | Nagoya/Kyushu | 7.0 | 13.8 % |
| PD10 | ISS | 4.3 | 4.4 % |
| PD11 | Nagoya/Kyushu | 5.1 | 7.1 % |
| PD12 | Nagoya/Kyushu | 4.8 | 6.7 % |
| PD13 | ISS | 4.4 | 12.2 % |
| PD14 | ISS | 4.4 | 6.3 % |
| PD16 | Nagoya/Kyushu | 4.7 | 12.9 % |
| PD18 | Nagoya/Kyushu | 4.9 | 19.4 % |
| PD19 | ISS | 6.0 | 7.2 % |
| PD22 | METU | 6.1 | 11.6 % |
| PD24 | Nagoya/Kyushu | 4.6 | 65.6 % |
| PD26 | ISS | 6.2 | 48.0 % |
| PD27 | Nagoya/Kyushu | 5.4 | 9.0 % |

### 4.1.3 Vertexing

After linking of base-tracks, tracks are selected for vertexing. For this purpose tracks with angle tan$\theta \leq 0.4$ rad are used. If there are more 4 or more tracks in a specified area which converge to a single point, it is selected as vertex. Corresponding mother proton is then searched at most 3 $\mu$m from vertex point. If the mother proton is found according to beam angle and position, this interaction will be defined as primary proton interaction.

Due to different densities of different materials used in experiment which are tungsten, emulsion and plastic layer, most of the vertices are found inside the tungsten target. In addition, emulsion layers has higher density with respect to plastic layers which results in more vertices inside emulsion layers then plastic layers. Figure(4.6) shows distribution of vertices according to Z direction which is expected due to the

density difference between materials used.

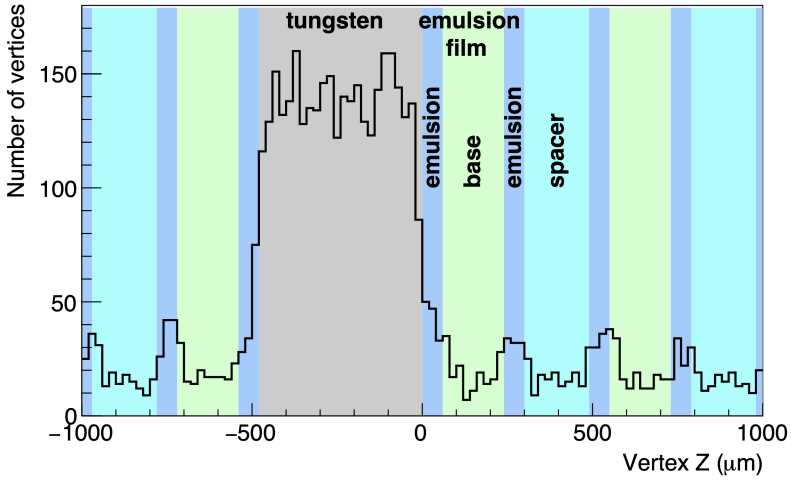


Figure 4.6: Distribution of vertices according to Z-direction

The track multiplicity in data and MC is compared as shown in Figure (4.7). Although the shape of distributions look consistent, there are discrepancies.

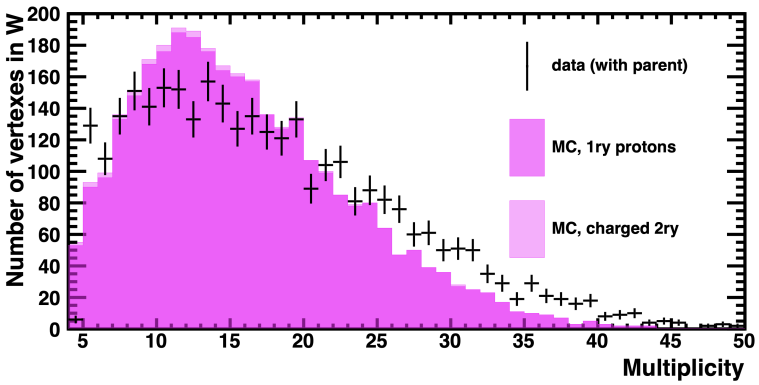


Figure 4.7: Comparison of multiplicty for data and FLUKA simulation

### 4.1.4 Decay Search

Finding topologically similar decays to short-lived particles are done by selection criteria which requires flight length of $D_s \geq 2$ emulsion layers and $\leq 5$ mm, flight length of $\tau \geq 2$ emulsion layers and $\leq 5$ mm, $\Delta\theta_{D_s \to \tau} \geq 2$ mrad, $\Delta\theta_{\tau \to X} \geq 15$ mrad and flight length of charm pair $\geq 0.1$ mm and $\leq 5$ mm (charged decays with $\Delta\theta \geq$

15 mrad or neutral decays).

Table 4.3: Number of vertices found and decay search results in tungsten for a sample of data and FLUKA simulation.

| | Expected | Observed |
|---|---|---|
| Vertices in tungsten target | 28390 $\pm$ 910 (syst.) | 29297 |
| Double decay topology | 15.9 $\pm$ 3.5 | 20 |

Number of found double decay topology and number of found vertices in tungsten target from a selected part of data is compared with FLUKA simulation and they are in good agreement according to Table 4.3, the systematic uncertainty in simulation can be explained due to the thickness uncertainty of tungsten plates. With selection criteria, decay candidates for double charm events are found and one example shown in Figure 4.8.

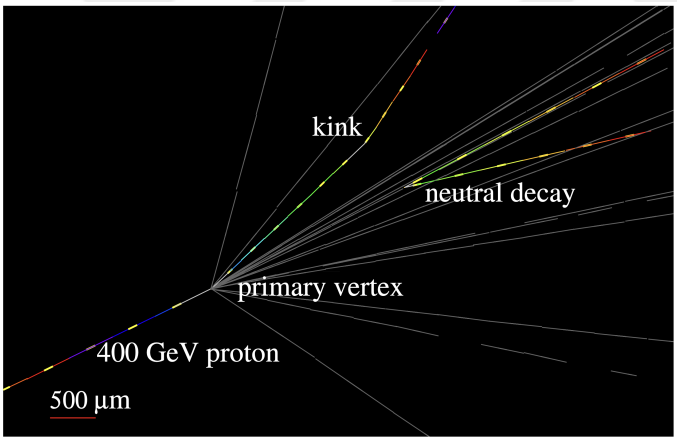


Figure 4.8: Double kink example

## 4.2 Improvement of Tracking

Tracking algorithm calculates chi-square for each reconstructed track according to Equation(4.3). Each two neighbour segments from a track is extrapolated to the middle of their Z positions according to their slopes. Then the difference between their extrapolated positions to this middle Z position, in X and Y directions are defined as

$\Delta$X and $\Delta$Y respectively. For angular difference, difference in X and Y components of slopes of two neighbouring segments is calculated and defined as $\Delta\theta_X$ and $\Delta\theta_Y$ respectively.

For pilot run position and angular resolutions in X and Y directions are defined as $\sigma_X$, $\sigma_Y$, $\sigma_{\theta_X}$ and $\sigma_{\theta_Y}$ and they are obtained test beam data as constants. Position resolution is taken as 2 $\mu$m while angular resolution is taken as 5 mrad. In order to improve tracking, these position and angular resolutions can be obtained for each module from data.

$$\chi^2 = \frac{\Delta X^2}{{\sigma_X}^2} + \frac{\Delta Y^2}{{\sigma_Y}^2} + \frac{{\Delta\theta_X}^2}{{\sigma_{\theta_X}}^2} + \frac{{\Delta\theta_Y}^2}{{\sigma_{\theta_Y}}^2} \tag{4.3}$$

### 4.2.1 Data samples

For tracking resolution study, a sub-sample of PD10 module is used in the analysis. In order to produce MC data, FLUKA is used as an event generator. The generated events are passed through GEANT4 in order to simulate the particle passage through the detector. A sub-volume of module is simulated that corresponds 3 tungsten and 30 emulsion films. The number of segments in data and MC is shown in Table 4.4.

Table 4.4: Number of segments and number of tracks in data and MC samples.

| | Details | # of Tracks | # of Segments |
|---|---|---|---|
| Data | PD10 | 741828 | 7939995 |
| MC | FLUKA | 519845 | 8462247 |

### 4.2.2 Position and angular resolutions

To obtain position and angular resolutions, each track is fitted to a line and their slopes with respect to Z-directions are calculated (Figure 4.9). From these slopes and Z-positions, X and Y positions for each segment are calculated. Figure 4.10 shows difference between calculated and reconstructed positions. Then, a Gaussian fit is applied to this distribution to obtain position resolutions in X and Y directions.

High momentum proton tracks which have information for all 30 segments in their tracks are selected. Position resolutions for them is also measured from Figure 4.11. Measured position resolutions are given in Table 4.5.

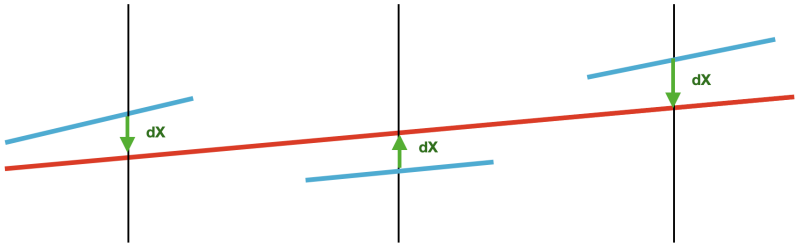


Figure 4.9: Calculation of $\Delta X$ and $\Delta Y$ from track fit.

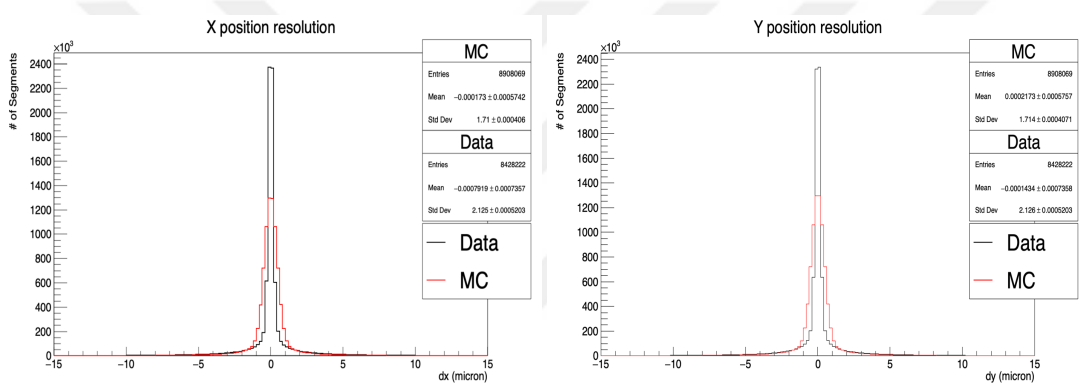


Figure 4.10: Distribution of difference between observed and expected X (Y) positions from track fit in left (right).

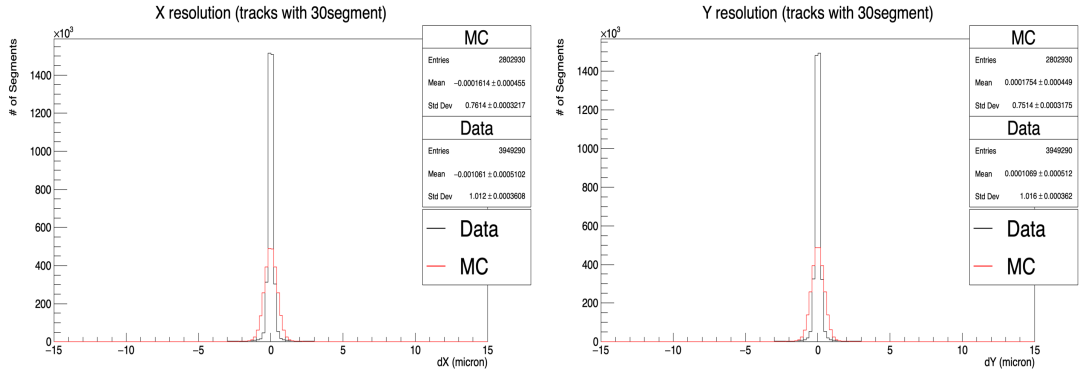


Figure 4.11: Distribution of difference between observed and expected X (Y) positions from track fit in left (right) for high momentum tracks.

Table 4.5: Position resolutions for all tracks and for high momentum tracks.

| All Tracks | | |
|---|---|---|
| Position resolution: | $\sigma_X$ | $\sigma_Y$ |
| Data | 2.125 $\mu$m | 2.126 $\mu$m |
| MC | 1.71 $\mu$m | 1.714 $\mu$m |
| High Momentum Tracks | | |
| Position resolution: | $\sigma_X$ | $\sigma_Y$ |
| Data | 1.012 $\mu$m | 1.016 $\mu$m |
| MC | 0.7614 $\mu$m | 0.7514 $\mu$m |

Similarly for angular resolutions, $\theta_X$ and $\theta_Y$ are calculated from track fit. The difference between fitted and reconstructed slopes is calculated. A Gaussian fit is applied to this distribution to obtain angular resolutions (Figure 4.12). Angular resolutions are also estimated for the high momentum proton tracks (Figure 4.13). Measured angular resolutions are given in Table 4.6 for $\sigma_{\theta_X}$ and $\sigma_{\theta_Y}$.

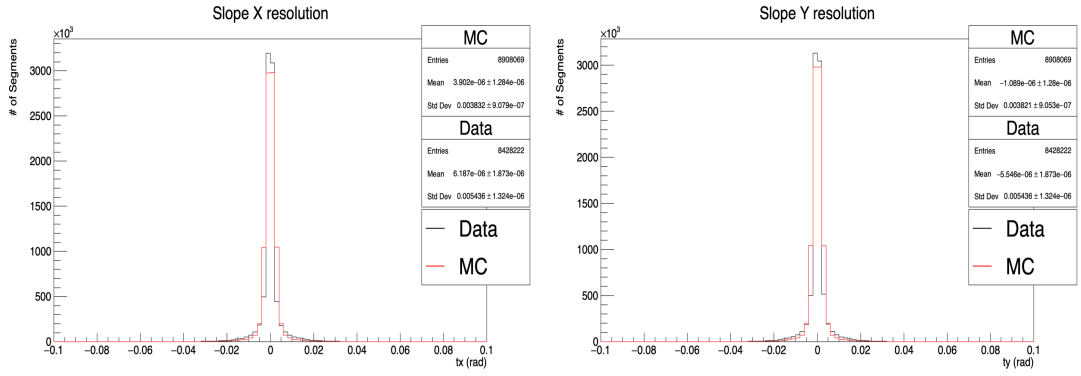


Figure 4.12: Distribution of difference between observed and expected $\theta_X$ ($\theta_Y$) angles from track fit in left (right)

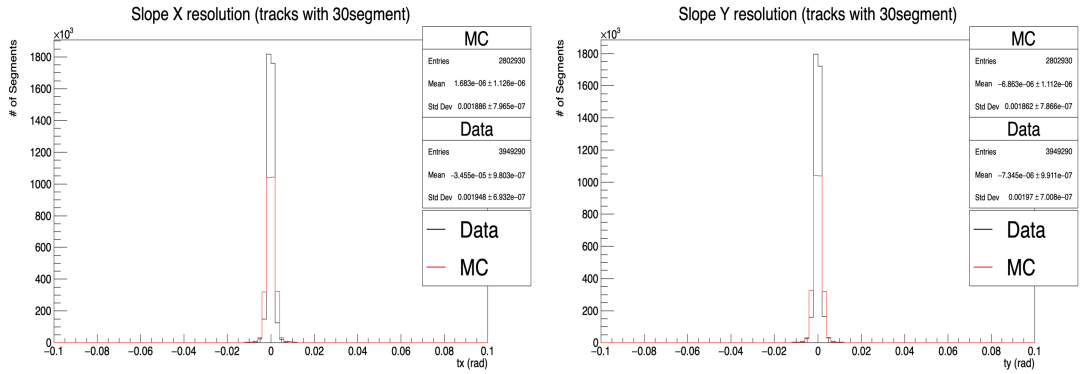


Figure 4.13: Distribution of difference between observed and expected $\theta_X$ ($\theta_Y$) angles from track fit in left (right) for high momentum tracks

Table 4.6: Angular resolutions for all tracks and for high momentum tracks.

| All Tracks | | |
|---|---|---|
| Angular resolution: | $\sigma_{\theta_X}$ | $\sigma_{\theta_Y}$ |
| Data | 5.436 mrad | 5.436 mrad |
| MC | 3.832 mrad | 3.821 mrad |
| **High Momentum Tracks** | | |
| Angular resolution: | $\sigma_{\theta_X}$ | $\sigma_{\theta_Y}$ |
| Data | 1.948 mrad | 1.970 mrad |
| MC | 1.886 mrad | 1.862 mrad |

### 4.2.3 $\chi^2$ Results

After obtaining position and angular resolutions, $\chi^2$ of track fit is estimated. Figure 4.14 shows $\Delta X^2/{\sigma_X}^2$ and $\Delta Y^2/{\sigma_Y}^2$ distributions with position resolutions from Table 4.5. Similarly, Figure 4.15 shows $\Delta {\theta_X}^2/{\sigma_{\theta_X}}^2$ and $\Delta {\theta_Y}^2/{\sigma_{\theta_Y}}^2$ distributions with angular resolutions from Table 4.6.

Similarly using position and angular resolutions measured from high momentum proton tracks, Figure 4.16 shows $\Delta X^2/{\sigma_X}^2$ and $\Delta Y^2/{\sigma_Y}^2$ distributions while Figure 4.17 shows $\Delta {\theta_X}^2/{\sigma_{\theta_X}}^2$ and $\Delta {\theta_Y}^2/{\sigma_{\theta_Y}}^2$ distributions.

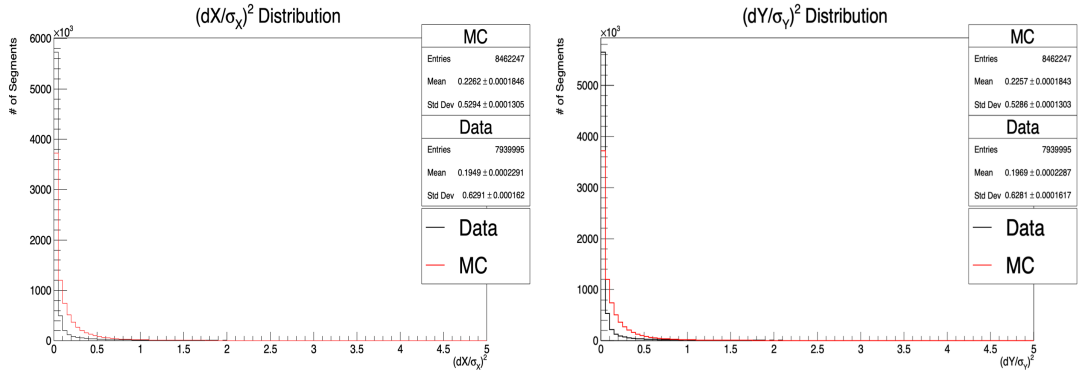


Figure 4.14: $\Delta X^2/{\sigma_X}^2$ (left) and $\Delta Y^2/{\sigma_Y}^2$ (right) distributions with position resolutions from Table 4.5.

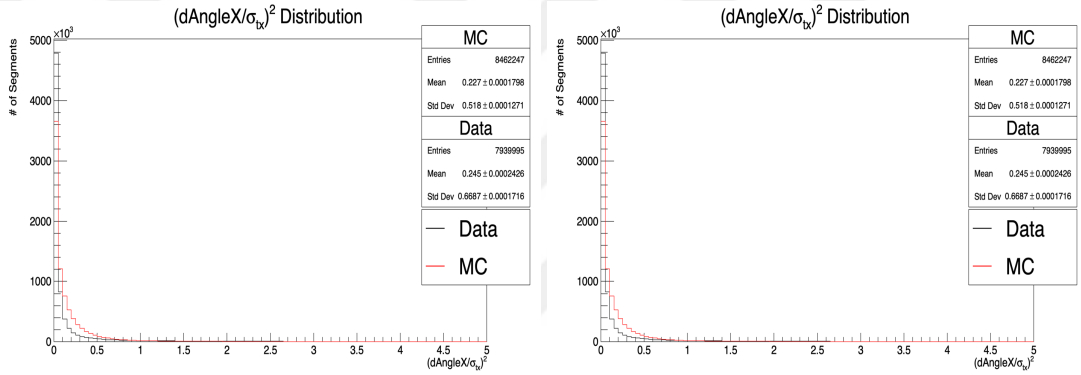


Figure 4.15: ${\Delta\theta_X}^2/{\sigma_{\theta_X}}^2$ (left) and ${\Delta\theta_Y}^2/{\sigma_{\theta_Y}}^2$ (right) distributions with angular resolutions from Table 4.6.

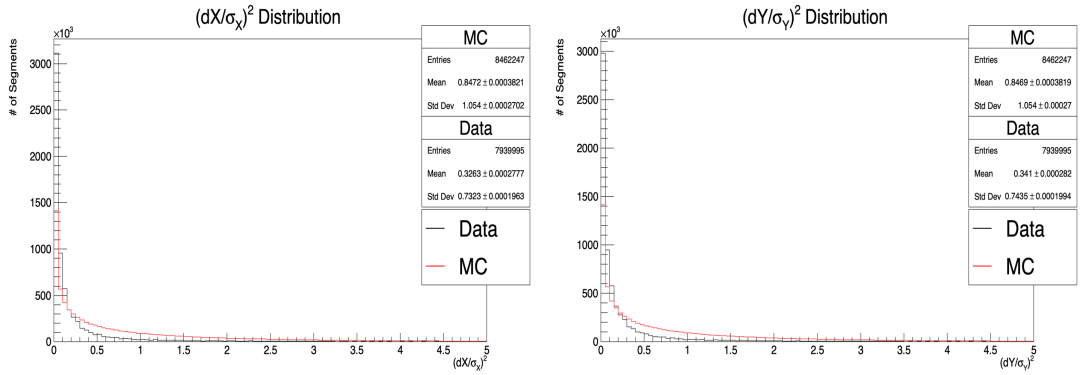


Figure 4.16: $\Delta X^2/{\sigma_X}^2$ (left) and $\Delta Y^2/{\sigma_Y}^2$ (right) distributions with position resolutions from Table 4.5 for high momentum tracks.

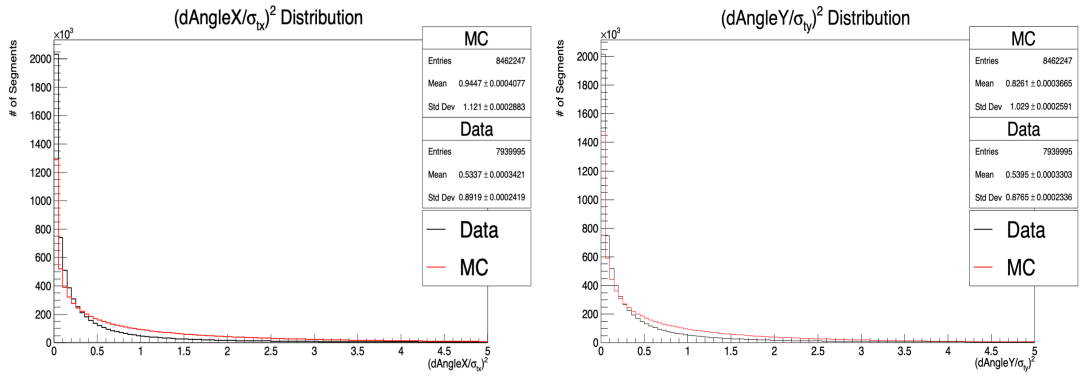


Figure 4.17: ${\Delta\theta_X}^2/{\sigma_{\theta_X}}^2$ (left) and ${\Delta\theta_Y}^2/{\sigma_{\theta_Y}}^2$ (right) distributions with angular resolutions from Table 4.6 for high momentum tracks.

After calculation each resolution term in Equation 4.3, $\chi^2$ is estimated as shown in Figure 4.18. The same estimation is also done for high energy proton tracks shown in Figure 4.19.

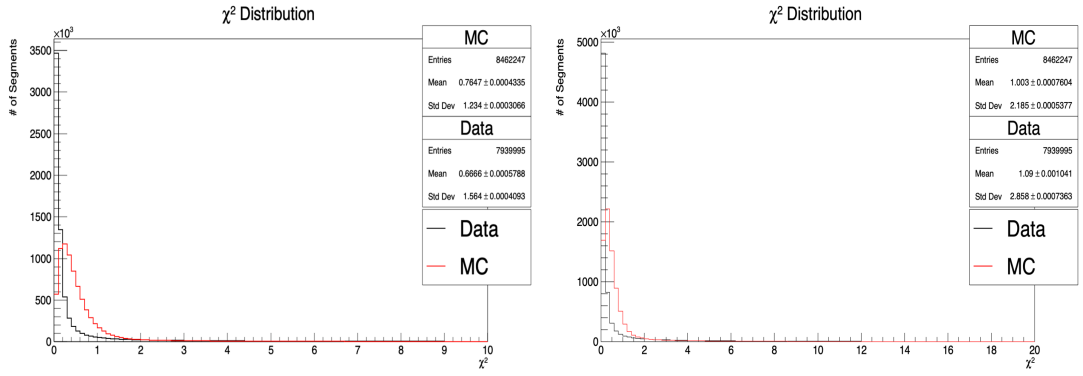


Figure 4.18: $\chi^2$ distribution from resolutions obtained by all tracks between 0-10 (left) and 0-20 (right).

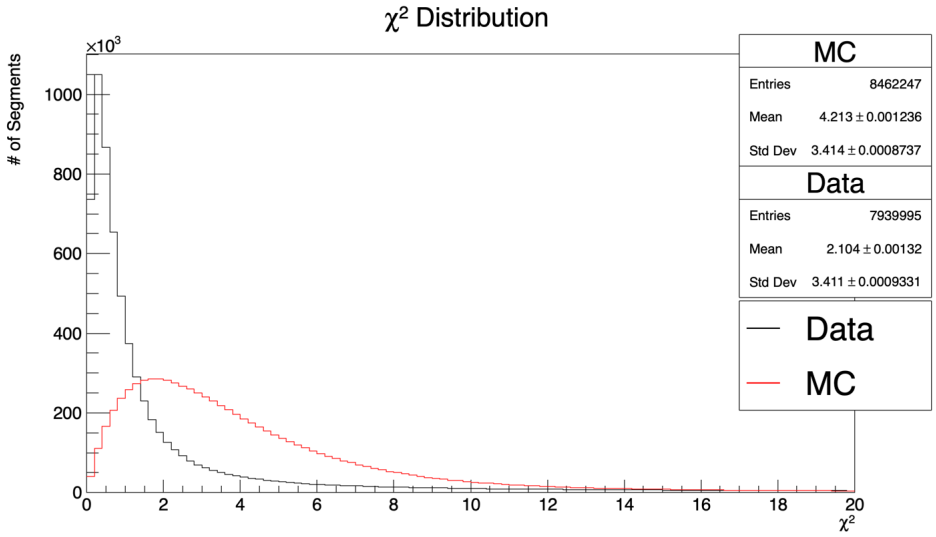


Figure 4.19: $\chi^2$ distribution from resolutions obtained by high momentum tracks.

A threshold is determined for $\chi^2$ to eliminate miss-reconstructed segments (Figure 4.20). Tracks that has at least one miss-reconstructed segment are rejected. Rejected tracks and their percentages are summarized in Table (4.7) for both data and MC sample.

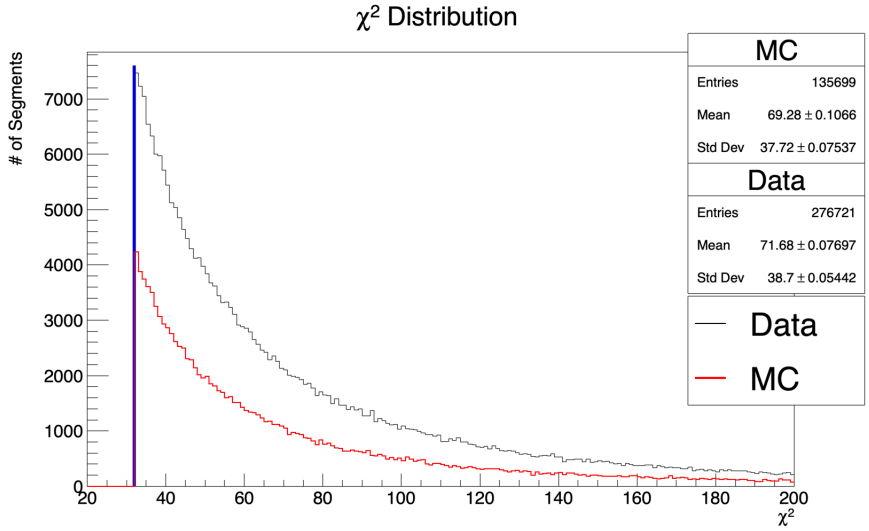


Figure 4.20: $\chi^2$ distribution of segments that has larger $\chi^2$ than acceptance threshold.

As mentioned earlier, the detection of $D_s$ decay requires very high position and angular resolutions. Therefore, the tracking in DsTau is very crucial part of the event

Table 4.7: Number of rejected segments and tracks with their percentages with respect to all tracks and segments.

| | Number of all segments | Number of rejected segments | Percentage of rejected segments |
|---|---|---|---|
| Data sample | 7939995 | 276721 | 3.485 % |
| MC sample | 8462247 | 135699 | 1.604 % |
| | # of all tracks | # of rejected tracks | Percentage of rejected tracks |
| Data sample | 741828 | 85303 | 11.499 % |
| MC sample | 519845 | 43816 | 8.429 % |

reconstruction. Therefore, tracking resolution must be studied for a possible improvement.

For this purpose tracks that does not satisfy $\chi^2$ requirements are rejected. While 11.5 % of tracks from data sample is rejected due to $\chi^2$ threshold, 8.429 % of tracks are rejected from MC sample. In conclusion preliminary results of $\chi^2$ distribution, shows that tracking efficiency is lower for data sample. This result is expected due to high track density which makes it difficult distinguish near segments.

# CHAPTER 5

# LIFETIME MEASUREMENT

Decay length (flight length) is the distance that a particle travel until it decays (Figure 3.6). Tracking with nuclear emulsion technique makes the measurement of position information for particles precise in micrometers. With this information DsTau can measure decay lengths of particles at high precision but tracking with nuclear emulsion technique do not have any time information for particles which is needed for life time measurement of particles.

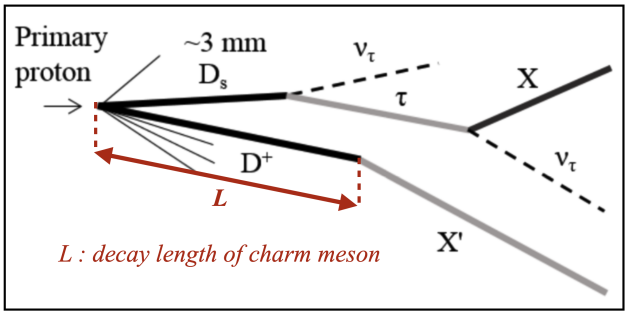


Figure 5.1: Decay topology of $D_s$.

## 5.1 Introduction

To measure life time of a particle momentum information of the particle can be used to estimate the velocity of the particle. It is possible to measure the lifetime of the particles if both momentum and flight length information have measured accurately.

Two different designs are made for momentum measurement of the particles in the DsTau experiment. While first design uses ECC which is using 26 emulsion plates separated by 25 plates of 1 mm lead, later design suggests 25 emulsion plates sepa-

rated with 3 plates of 0.5 mm tungsten. The second design will be used for physics run in 2021 and 2022 but their vertexing data is not ready for time being. Also a study is currently ongoing for the momentum measurement which uses current tracking data and measure momentum of particles by multiple coulomb scattering. For 2018 test run particles we do not have any momentum information.

For preliminary measurement of lifetime of charm mesons, momentum information can be obtained using simulated Monte Carlo (MC) events with similar topologies. For this purpose total of 50 million 400 GeV proton-proton events generated using PYTHIA8 Monte Carlo Event Generator [17].

After getting momentum information of the particle, decay length method can be used to measure mean lifetime of particles using equations (5.1) and (5.2) [18].

$$c \cdot \tau = \vec{L} \cdot \vec{p}_{parent} \cdot \frac{m_{parent}}{\mid p_{parent} \mid^2} \tag{5.1}$$

$$\overline{\tau} = \frac{m_{parent}}{p_{parent}} \cdot \frac{\overline{L}}{c} \tag{5.2}$$

Where $c$ is the speed of light, and $\tau$ is the life time of the particles. $\overline{L}$ is the mean decay length of the particles. Mass and momentum of the charmed particles are $m$ and $p$ respectively.

## 5.2 Data Selection

2018 test run data is used for the analysis in this study. After track reconstruction is applied, vertexes are found using vertexing algorithm. To find double kink topology which is needed to obtain $D_s$ to $\tau$ decays from proton-proton interactions, selection criteria in Table(5.1) is applied to all vertexes.

After applying selection criteria a total of 169 events are selected from PD03 and PD04 modules as $D_s$ to $\tau$ canditates. These 169 candidate events are then classified as 1-prong and 2-prong which are the number of charged daughter particles of charm meson. A candidate event is visualized by Event Display Analyzer in Figure (5.2) where the kink angle is 66 mrad and the flight length of the parent track is 3.73 mm.

Table 5.1: Selection criteria for double kink $D_s \rightarrow \tau \rightarrow X$

| Selection Criteria |
|---|
| (1) Flight length of $D_s \geq 2$ emulsion layers |
| (2) Flight length of $\tau \geq 2$ emulsion layers and $\Delta\theta_{D_s \rightarrow \tau} \geq 2$ mrad |
| (3) Flight length of $D_s < 5$ mm and flight length of $\tau < 5$ mm |
| (4) $\Delta\theta_{\tau \rightarrow X} \geq 15$ mrad |
| (5) Pair charm: 0.1 mm $\leq$ flight length $< 5$ mm<br>(charged decays with $\Delta\theta \geq 15$ mrad or neutral decays) |

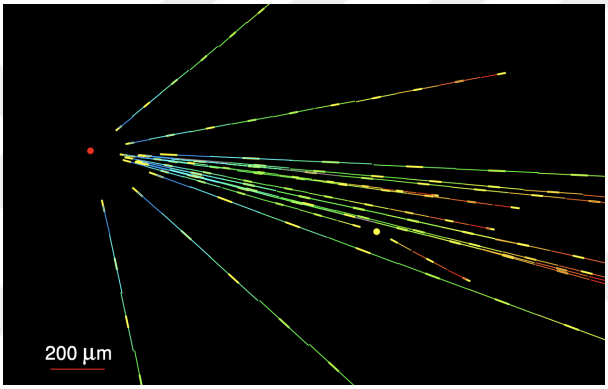


Figure 5.2: Event display of a charmed decay candidate.

105 of these 169 decay candidates are 1-prong charged charm mesons and 64 of them are 2-prong neutral charm mesons. Distributions of slopes of charm mesons are shown in Figure(5.3) and in Figure(5.4) separately for 1-prong and 2-prong events.

For topological similarity between generated Monte Carlo events and charm candidate events flight length and kink angles for 1-prong events are used while for 2-prong events flight length and opening angles are used. Figure(5.5) shows flight length distributions in mm. Kink angle distributions and opening angle distributions are represented for 1-prong events and 2-prong events respectively in Figure(5.6).

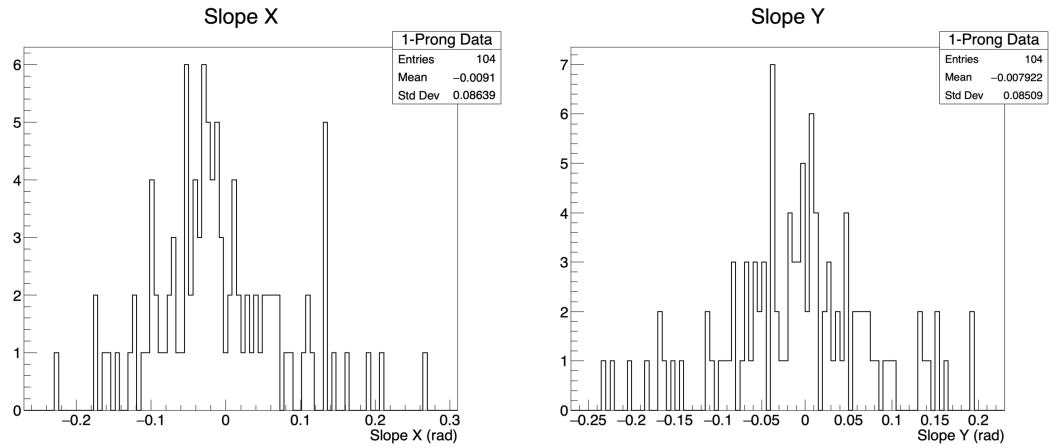


Figure 5.3: Slope distributions in X-direction (left) and in Y-direction (right) for 1-prong events.

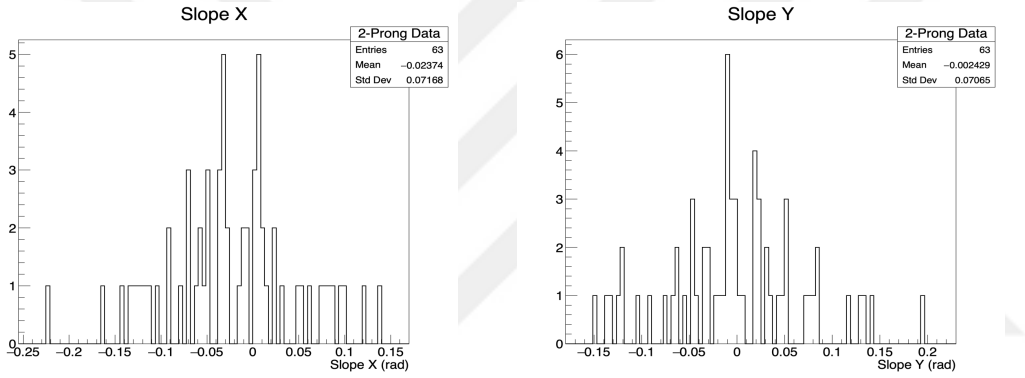


Figure 5.4: Slope distributions in X-direction (left) and in Y-direction (right) for 2-prong events.

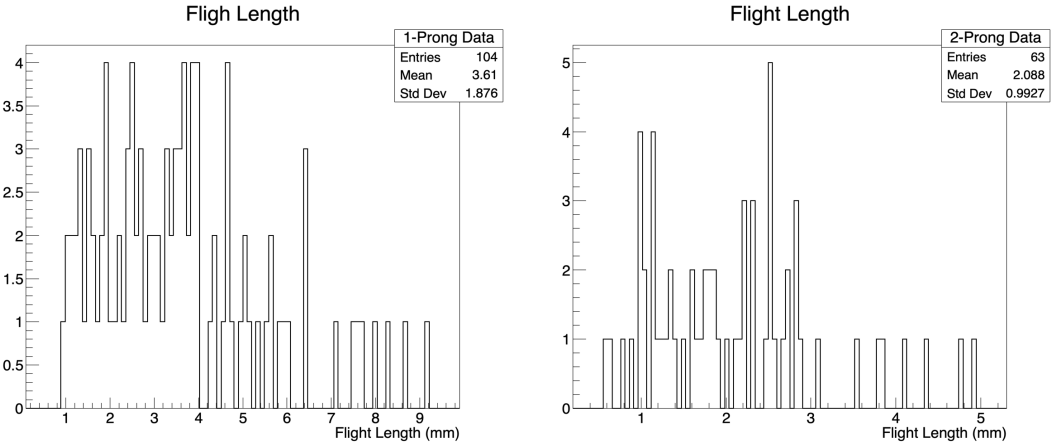


Figure 5.5: Flight length distributions for 1-prong (left) and 2-prong (right) events.

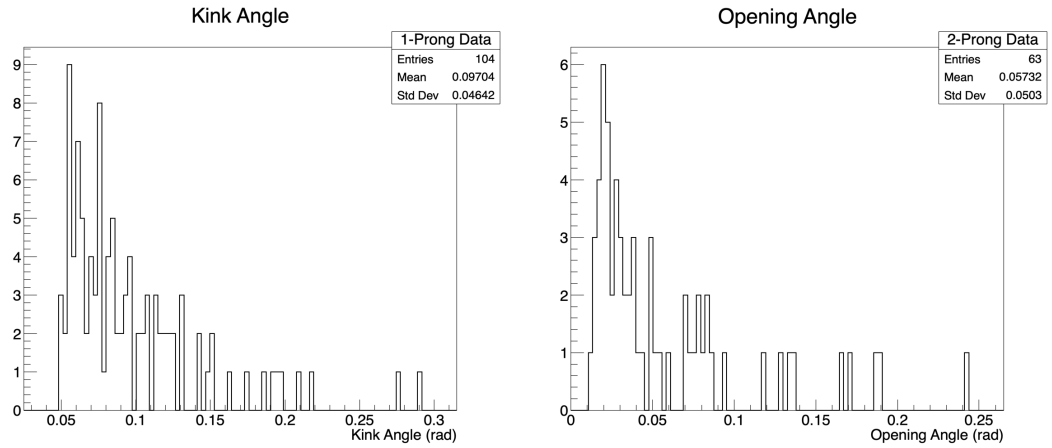


Figure 5.6: Kink angle distribution for 1-prong events (left) and opening angle distribution for 2-prong events (right).

## 5.3 Monte Carlo Simulation

PYTHIA8 event generator is used to generate $50 \times 10^6$ double charm events at 400 GeV proton interactions, distributions of these charmed particles are shown in Table(5.2) and Table(5.3) separately for particles having $c$ and $\bar{c}$.

Table 5.2: Charm meson distributions of $50 \times 10^6$ double charm events with second charm particle having $c$ quark

| | | 1. Charm ID | | | |
|---|---|---|---|---|---|
| | | $D^-$ | $\overline{D}^0$ | $D_s^-$ | Total |
| 2. Charm ID | $D^+$ | 3.907 % | 5.003 % | 0.741 % | 9.651 % |
| | $D^0$ | 10.352 % | 16.019 % | 2.214 % | 28.585 % |
| | $D_s^+$ | 1.339 % | 1.984 % | 0.334 % | 3.657 % |
| | Total | 15.598 % | 23.006 % | 3.289 % | 41.893 % |

From simulated $50 \times 10^6$ events total of $27.6 \times 10^6$ events have two charm particles decaying with 1-prong and 2-prong decay modes. 1-prong and 2-prong events are separated using the charge of charm meson. If charm meson has one charged daughter it can only be a charged charm particle with 1-prong otherwise if it has two charged daughter it is a neutral charm particle with 2-prong. Particle IDs of charm particles

Table 5.3: Charm meson distributions of $50 \times 10^6$ double charm events with second charm particle having $\bar{c}$ anti-quark

| | | 1. Charm ID | | | |
|---|---|---|---|---|---|
| | | $D^+$ | $D^0$ | $D_s^+$ | Total |
| 2. Charm ID | $D^-$ | 3.372 % | 3.907 % | 0.640 % | 7.919 % |
| | $\overline{D}^0$ | 9.481 % | 13.750 % | 2.078 % | 25.309 % |
| | $D_s^-$ | 1.140 % | 1.586 % | 0.401 % | 3.127 % |
| | Total | 13.993 % | 19.243 % | 3.119 % | 36.355 % |

are shown in Figure(5.7). Table(5.4) shows distributions of charm mesons and their number of occurrences and their fractions.

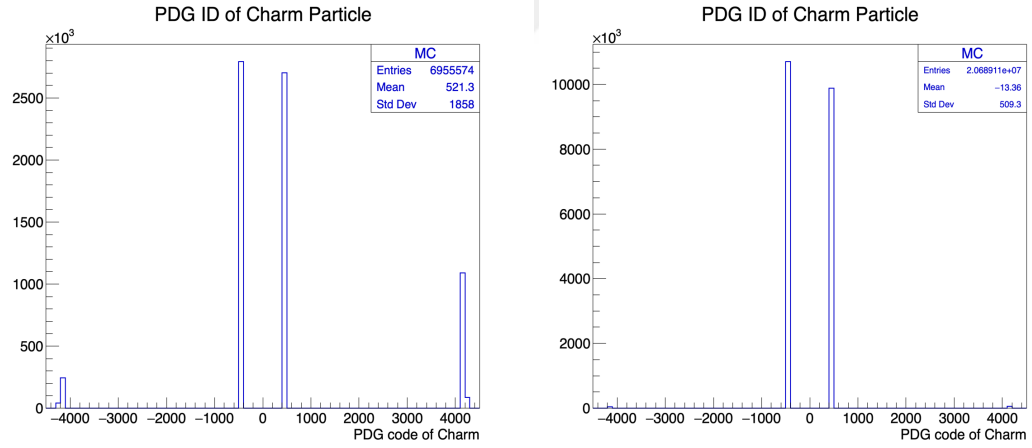


Figure 5.7: PDG code of charm particles for 1-prong (left) and 2-prong (right) events.

Flight length distributions of PYTHIA sample is shown in Figure(5.8). Kink angle distribution for 1-prong events and opening angle distributions for 2-prong events are also shown in Figure(5.9).

Table 5.4: MC Charm events

| Decay mode | Particle | # of Charm Particles | % of Occurrence | % of events in total |
|---|---|---|---|---|
| 1-prong | | 6955574 | | 25.16 % |
| | $D^+$, $D^-$ | 3941444 | 56.67 % | 14.26 % |
| | $D_s^+$, $D_s^-$ | 1552267 | 22.32 % | 5.62 % |
| | $\Lambda_c^+$ | 1333564 | 19.17 % | 4.82 % |
| | $\Xi_c^+$ | 128299 | 1.84 % | 0.46 % |
| 2-prong | | 20689113 | | 74.84 % |
| | $D^0$, $\overline{D}^0$ | 20588357 | 99.51 % | 74.47 % |
| | $\Xi_c^0$ | 100756 | 0.49 % | 0.36 % |

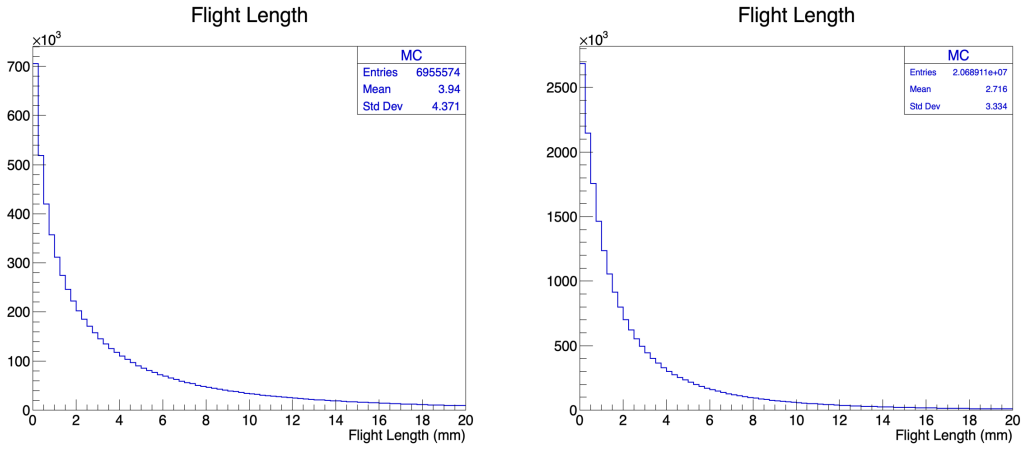


Figure 5.8: Flight length distributions for 1-prong (left) and 2-prong (right) MC events.

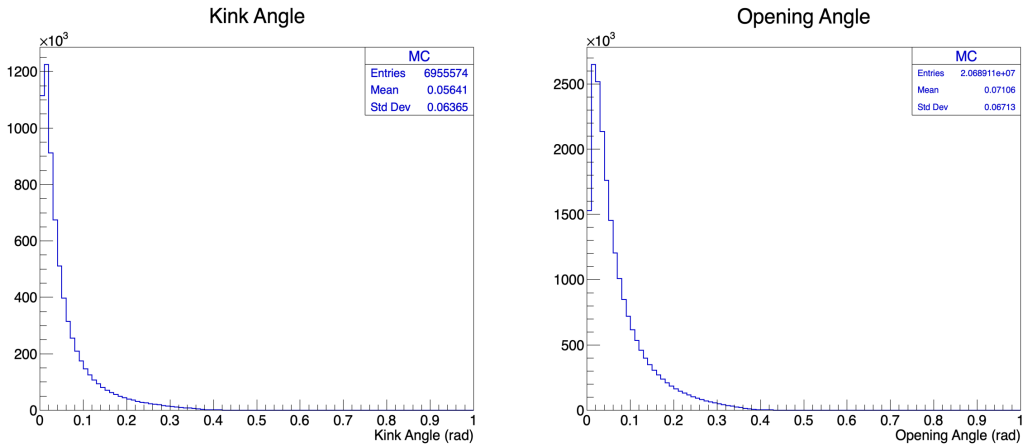


Figure 5.9: Kink angle distribution for 1-prong (left) and opening angle distribution for 2-prong (right) for Monte Carlo events.

From equations (5.1) and (5.2) lifetime of particles calculated as Monte Carlo sample has momentum information and their distributions shown in Figure(5.10). Mean lifetime for charged and neutral charm particles are 695.4 and 408.3 femtosecond respectively.

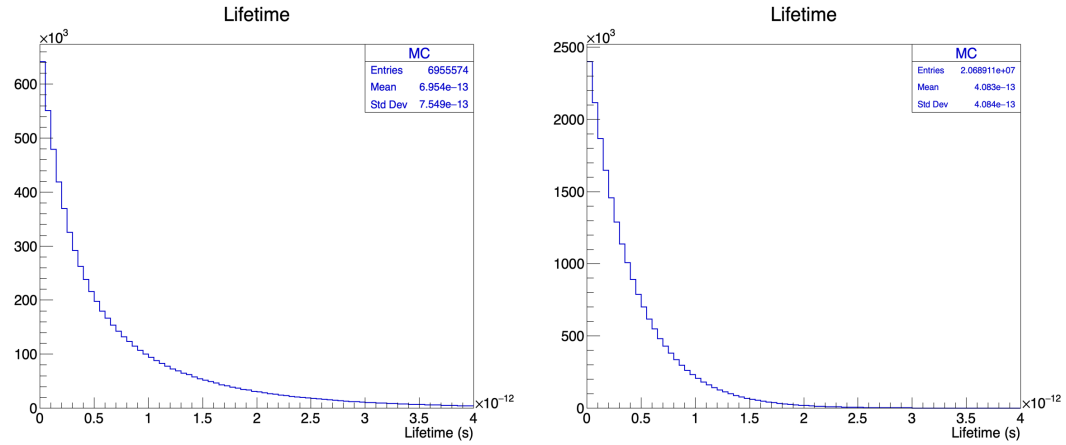


Figure 5.10: Calculated Lifetime distributions for 1-prong (left) and 2-prong (right) for MC events.

## 5.4 Lifetime estimation

To estimate the lifetime of a charm decay candidate, similar events are selected from 27 million MC events according to their multiplicity, flight length, kink angle, and opening angle. This process is repeated for all 169 charm decay candidates. While 105 1-prong decays have a kink angle, 64 2-prong decays have an opening angle for selection. Acceptance ranges for these 4 properties are given as follows;

- Multiplicity must be $\pm 1$ of multiplicity of decay candidate.
- Flight length of charmed particle must be $\pm 0.01\ mm$ of the flight length of the charmed particle of decay candidate
- The kink angle must be $\pm 5\ mrad$ from the kink angle of 1-prong decay.
- The opening angle must be $\pm 5\ mrad$ from the opening angle of 2-prong decay.

Lifetime estimation for a 1-prong event which has 3.634 mm of flight length and 0.08434 rad kink angle, Monte Carlo events are chosen (Figure 5.11). Total of 41 events are selected for this sample event which have life time distribution in (Figure 5.12). In conclusion life time of charm pair meson for this event has been estimated as 1089 fs. This estimation is recalculated for each 105 1-prong candidate event and their mean is calculated for the mean life time of 1-prong charm particles.

To get a more precise estimate for lifetime, two more selection criteria is applied to MC charmed sample. To get similar decay topology as $D_s$ to $\tau$ decay, pair charm particle should have flight length between 0.5 mm and 5 mm while kink angle (1-prong) or opening angle (2-prong) should be larger then 20 milliradian (Table 5.5).

Table 5.5: Selection criteria for pair charm

| Selection Criteria for pair charm |
|---|
| (1) Pair charm: 0.5 mm $\leq$ flight length $<$ 5 mm |
| (2) $\Delta\theta \geq$ 20 mrad |

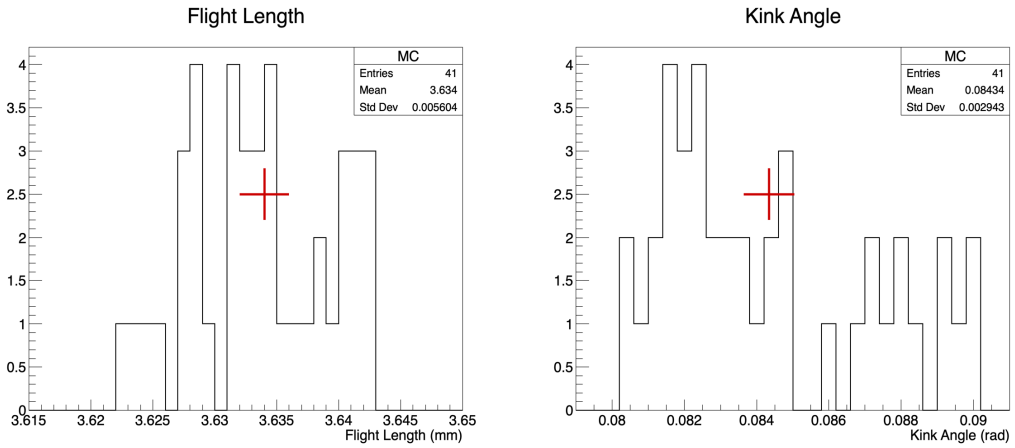


Figure 5.11: Estimation for sample 1-prong charm particle which has 3.634 mm of flight length and 0.08434 rad kink angle.

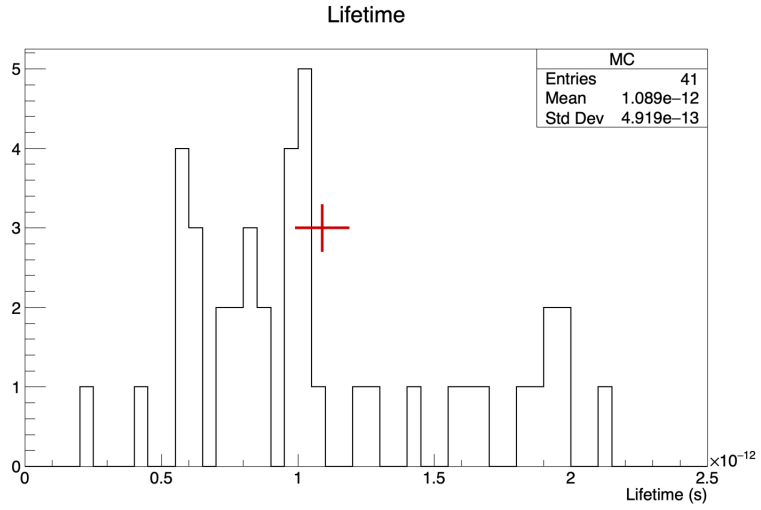


Figure 5.12: Estimation of lifetime for sample 1-prong charm particle which has 3.634 mm of flight length and 0.08434 rad kink angle.

Similarly lifetime estimation for a 2-prong candidate event which has flight length of 2.334 mm and opening angle between two daughters as 0.03895 rad, selection of Monte Carlo events are done (Figure 5.13). For this sample event 498 similar events are selected from $20.7 \times 10^6$ charm particles and this meson's lifetime is estimated as 407 fs (Figure 5.14).

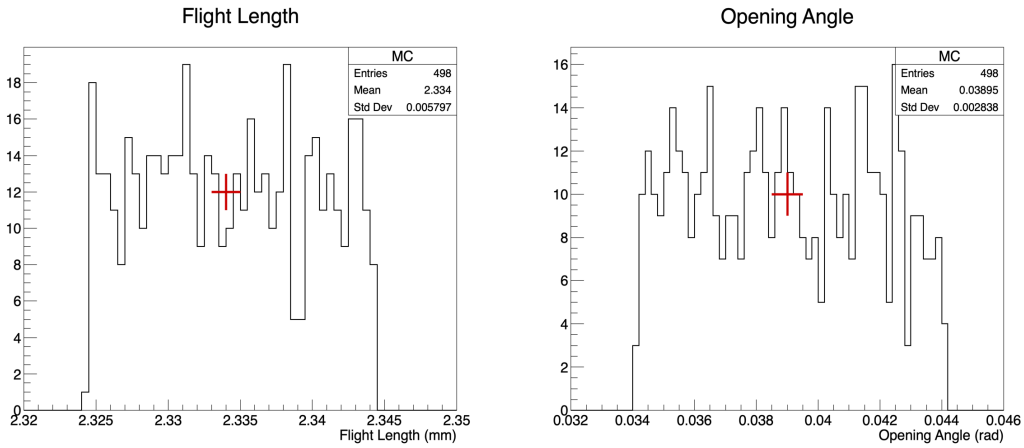


Figure 5.13: Estimation for sample 2-prong neutral charm particle which has 2.334 mm of flight length and 0.03895 rad opening angle.

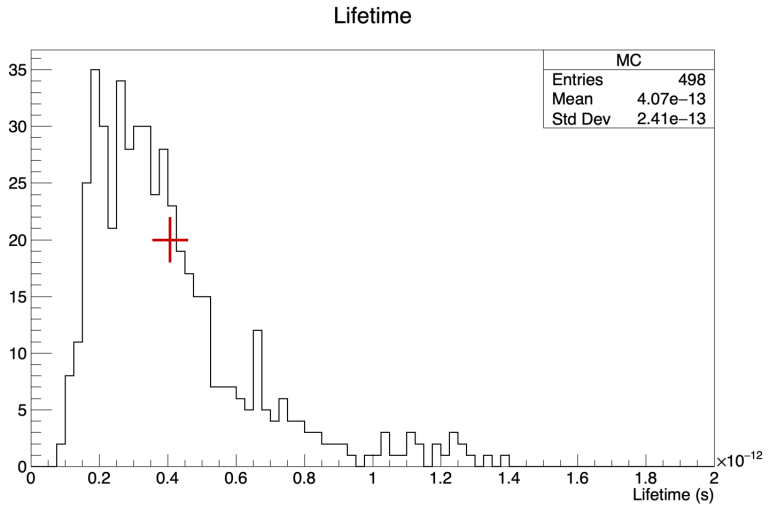


Figure 5.14: Estimation of Life Time for sample 2-prong neutral charm particle which has 2.334 mm of flight length and 0.03895 rad opening angle.

## 5.5 Results

From $7 \times 10^6$ 1-prong charged charm particles only 4663 charged charm particles selected for 105 1-prong decay candidate events. By applying selection criteria from Table(5.5) this number of charged charm particles decreased to 3314 (Table 5.6). Flight length and kink angle distributions with selection criteria applied are shown in

Figure(5.15) and Figure(5.16) for 1-prong events.

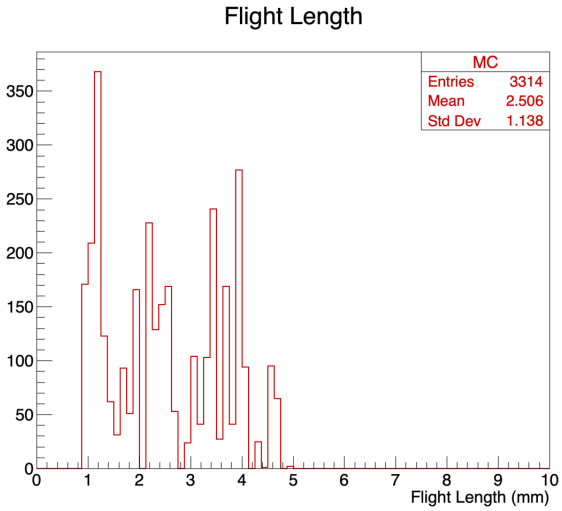


Figure 5.15: Flight length distributions with selection criteria (Table 5.5) for 1-prong

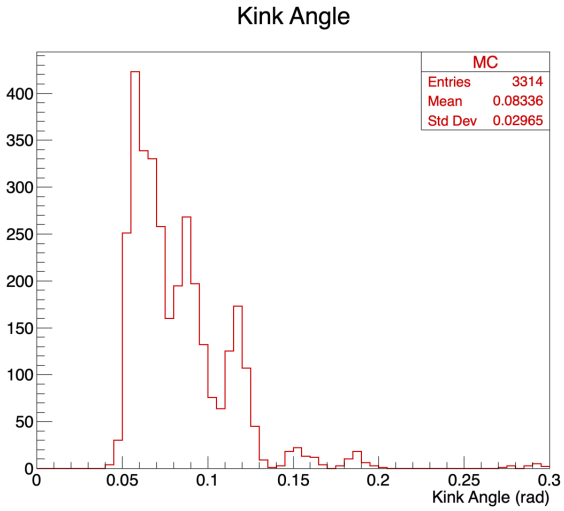


Figure 5.16: Kink angle distributions with selection criteria (Table 5.5) for 1-prong.

Similarly from $20.7 \times 10^6$ 2-prong neutral charm particles only 38462 neutral charm particles selected for 64 2-prong candidate events. By applying selection criteria from Table(5.5) this number of neutral charm particles decreased to 21843 (Table 5.6). Flight length and opening angle distributions with selection criteria applied are shown in Figure(5.17) and Figure(5.18) for 2-prong events.

Table 5.6: Selection of charmed events for lifetime estimation.

| Decay mode | # of events | # of events in acceptance range | # of events after selection criteria |
|---|---|---|---|
| 1-prong | $7 \times 10^6$ | 4663 | 3314 |
| 2-prong | $20.7 \times 10^6$ | 38462 | 21843 |

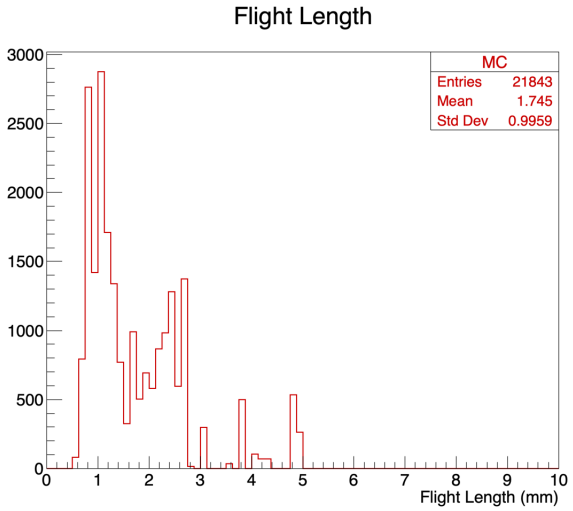


Figure 5.17: Flight length distributions with selection criteria (Table 5.5) for 2-prong

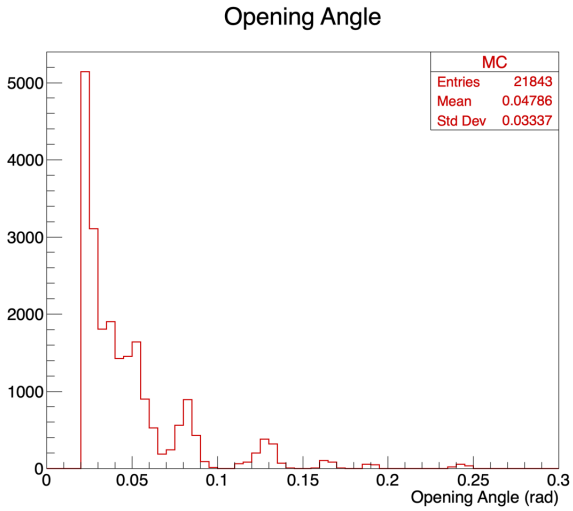


Figure 5.18: Opening angle distributions with selection criteria (Table 5.5) for 2-prong

To eliminate background events from charmed decay topology, selection criteria is

applied from Table(5.5). Lifetime distributions with and without selection criteria shown in Figure(5.19) and in Figure(5.20) respectively.

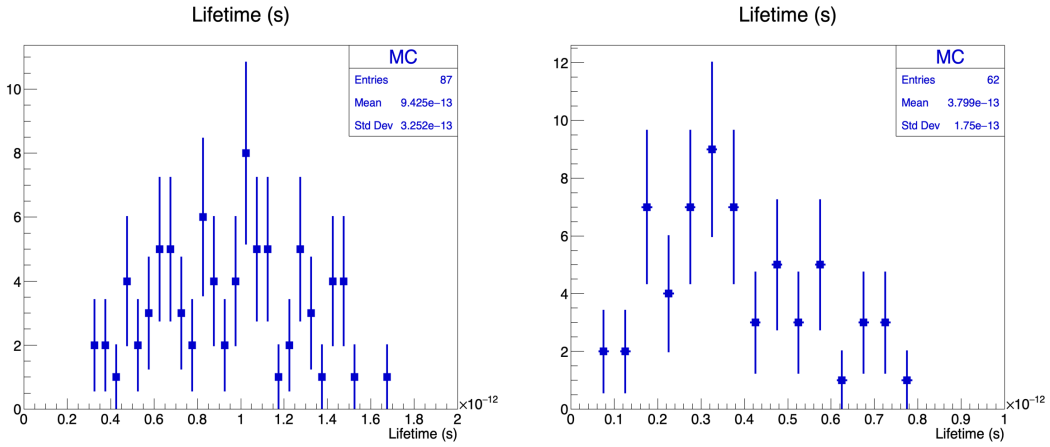


Figure 5.19: Lifetime distribution without selection criteria for 1-prong (left) and for 2-prong (right).

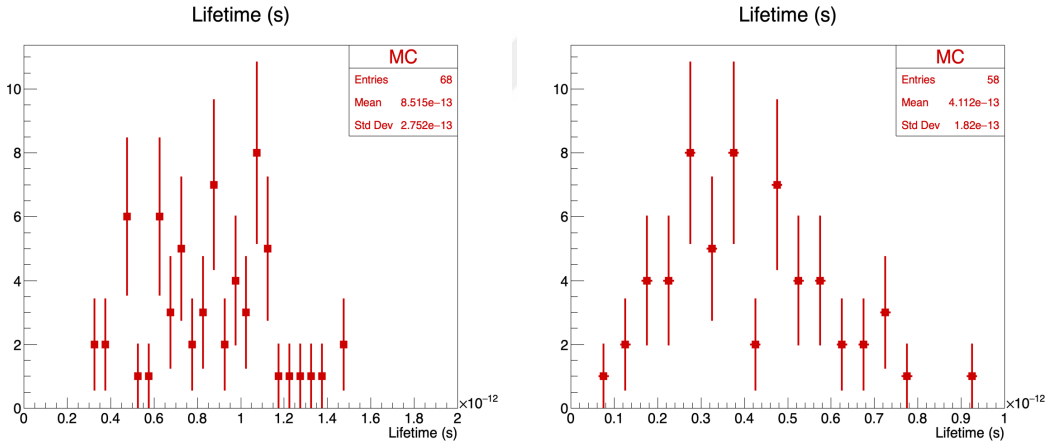


Figure 5.20: Lifetime distribution with selection criteria applied for 1-prong (left) and for 2-prong (right).

In conclusion, mean life time estimation for 1-prong decay mode of charged charm particles which are $D^+$, $D^-$, $D_s^+$, $D^-$, $\Lambda_c^+$ and $\Xi_c^+$ is 851.5 $\pm$ 33.3 femtoseconds. Charm lifetimes from previous experiments are shown more detailed in Table 5.7. According to their percentage occurrences in selected MC events, an expected mean lifetime can be calculated which is 744.86 $fs$. It can be said that this expected mean

lifetime is inside the uncertainty region of the measured lifetime value which is 851.5 $\pm$ 33.3 femtoseconds. Only having 105, two charm event candidates results in large uncertainties. Lifetime measurement for charged charmed particles should be updated with higher statistics.

Table 5.7: Distributions of 1-prong charged charm particles selected from generated MC events and lifetime of charged charm particles according to PDG.

| Particle | % of Occurrence | Lifetime ($fs$) |
|---|---|---|
| $D^+$, $D^-$ | 56.67 % | $1033 \pm 5\ fs$ |
| $D_s^+$, $D_s^-$ | 22.32 % | $504 \pm 4\ fs$ |
| $\Lambda_c^+$ | 19.17 % | $201.5 \pm 2.7\ fs$ |
| $\Xi_c^+$ | 1.84 % | $453 \pm 5\ fs$ |

Mean life time for 2-prong neutral charm particles which are $D^0$, $\overline{D}^0$ and $\Xi^0$ estimated as 411.2 $\pm$ 23.9 femtoseconds. For neutral charm particles it is known from Table(5.4) that 99.51 % of neutral charm particles are $D^0$, $\overline{D}^0$. In addition, $D^0$ and $\overline{D}^0$ decays in 2-prong decay mode (71 $\pm$ 6) % [19]. Previous measurement of lifetime of $D^0$, $\overline{D}^0$ was 410 $\pm$ 1.5 femtoseconds [19]. In conclusion measurement for lifetime of 2-prong decay mode of $D^0$ and $\overline{D}^0$ is in good agreement with the previous experimental results. This measurement can be improved with higher statistics and with momentum information of charmed particles from DsTau experiment.

$$\tau_{D^0} = 411.2 \pm 23.9 fs \tag{5.3}$$

# CHAPTER 6

# CONCLUSION

This thesis reports on a tracking resolution estimation and estimation of charmed particle lifetimes in the DsTau experiment.

The DsTau experiment is designed to measure differential cross section of $D_s$ which has short flight length and small kink angle. The detection of this unique decay topology requires very high resolution tracking detector. The only technology that presents sub-microns position resolution and a few mrad angular resolution is nuclear emulsion. The DsTau experiment has used nuclear emulsion based detector to detect short flight length and small angle decays. The tracking resolution of pilot run has been studied for proton tracks and also for primary vertex tracks. The tracking resolution obtained from data is compared with MC. In order to improve the tracking quality a selection criteria based on $\chi^2$ is developed and applied to the data. This selection disregards the miss reconstructed tracks thus improves the tracking purity.

Due to high position resolution of nuclear emulsion, it is possible to measure flight lengths of the particles with very high precision. Thus it makes measurement of lifetimes from data possible for short lived particles. But for the pilot run of DsTau experiment, there is no momentum information for particles which is a crucial part of lifetime measurement. To be able to simulate momentum information of charmed particles $50 \times 10^6$ events are generated with Pythia8 event generator which have 2 charmed particles in their final state. Then charmed events are classified as neutral and charged acording to decay topology. From these events some selection criteria is applied similar to DsTau experiments selection criteria for selection of double charm events like flight length and kink or opening angle.

For each 64 2-prong events and 105 1-prong double charm candidates, events with similar flight lengths, multiplicity and kink or opening angles are selected with high precision. From these selected events a mean lifetime is estimated for each event using MC events.

Although there is high uncertainties for the lifetime measurement due to low number of double charm candidates, the measurement of lifetime for $D^0$ found to be in good agreement with $411.2fs$ which has only 0.3 % error from the previous measurement. In conclusion this shows that the purity of $D^0$ sample is high but charged charm candidate suffers from background contamination.

This measurement can be improved with higher statistics which will be ready after the physics runs.

## REFERENCES


[1] M. K. Gaillard, P. D. Grannis, and F. J. Sciulli, "The standard model of particle physics," *Reviews of Modern Physics*, vol. 71, pp. S96–S111, mar 1999.

[2] R. Aaij *et al.*, "Test of lepton universality in beauty-quark decays," *Nature Phys.*, vol. 18, no. 3, pp. 277–282, 2022.

[3] S. Aoki *et al.*, "DsTau: Study of tau neutrino production with 400 GeV protons from the CERN-SPS," *JHEP*, vol. 01, p. 033, 2020.

[4] F. Vissani, "What is the standard model of elementary particles and why we have to modify it," *Italian Phys. Soc. Proc.*, vol. 73, pp. 117–135, 2001.

[5] F. Halzen and A. D. Martin, *QUARKS AND LEPTONS: AN INTRODUCTORY COURSE IN MODERN PARTICLE PHYSICS*. 1984.

[6] D. J. Griffiths, *Introduction to elementary particles; 2nd rev. version*. Physics textbook, New York, NY: Wiley, 2008.

[7] H. Pérez R., P. Kielanowski, and S. R. Juárez W, "Cabibbo–Kobayashi–Maskawa matrix: rephasing invariants and parameterizations," *J. Phys. Conf. Ser.*, vol. 485, p. 012058, 2014.

[8] S. M. Bilenky and J. Hosek, "GLASHOW-WEINBERG-SALAM THEORY OF ELECTROWEAK INTERACTIONS AND THE NEUTRAL CURRENTS," *Phys. Rept.*, vol. 90, pp. 73–157, 1982.

[9] C. Amsler, T. DeGrand, and B. Krusche, "Quark model," 09 2008.

[10] E. R. Cazaroto, V. P. Goncalves, F. S. Navarra, and M. Nielsen, "On the energy dependence of the $D^+/D^-$ production asymmetry," *Phys. Lett. B*, vol. 724, pp. 108–114, 2013.

[11] C. F. Wild, *Hadroproduction of D mesons in 400 GeV/c p-p interactions*. PhD thesis, Duke U., 1987.

[12] M. Artuso, B. Meadows, and A. A. Petrov, "Charm meson decays," *Annual Review of Nuclear and Particle Science*, vol. 58, no. 1, pp. 249–291, 2008.

[13] L. Gladilin, "Charm hadron production fractions," 12 1999.

[14] Y. Gornushkin, "Study of tau neutrino production in proton-nucleus interactions," *Journal of Physics: Conference Series*, vol. 1390, p. 012047, nov 2019.

[15] K. Kodama *et al.*, "Final tau-neutrino results from the DONuT experiment," *Phys. Rev. D*, vol. 78, p. 052002, 2008.

[16] S. Vasina, "Study of tau neutrino production with nuclear emulsion at CERN-SPS," *Journal of Physics: Conference Series*, vol. 2156, p. 012149, dec 2021.

[17] T. Sjöstrand, S. Ask, J. R. Christiansen, R. Corke, N. Desai, P. Ilten, S. Mrenna, S. Prestel, C. O. Rasmussen, and P. Z. Skands, "An introduction to PYTHIA 8.2," *Comput. Phys. Commun.*, vol. 191, pp. 159–177, 2015.

[18] K. Abe, I. Abt, C. Ahn, T. Akagi, N. Allen, W. Ash, D. Aston, K. Baird, C. Baltay, H. Band, M. Barakat, G. Baranko, O. Bardon, T. Barklow, A. Bazarko, R. Ben-David, A. Benvenuti, T. Bienz, G. M. Bilei, and T. Gillman, "Measurement of the tau lifetime at sld.," *Physical review D: Particles and fields*, vol. 52, pp. 4828–4838, 12 1995.

[19] K. A. Olive *et al.*, "Review of Particle Physics," *Chin. Phys. C*, vol. 38, p. 090001, 2014.